Journal of Trace Elements in Medicine and Biology 51 (2019) 176–190

Contents lists available at ScienceDirect

Journal of Trace Elements in Medicine and Biology

journal homepage: www.elsevier.com/locate/jtemb

Toxicology

In vitro apoptosis-induction, antiproliferative and BSA binding studies of a oxidovanadium(V) complex

Manasa Kongot[a], Neeraj Dohare[b,d], Dinesh S. Reddy[a], Neha Pereira[c], Rajan Patel[b], Mahesh Subramanian[c], Amit Kumar[a,*]

[a] Centre for Nano and Material Sciences, Jain (Deemed-to-be University), Jain Global Campus, Jakkasandra Post, Bengaluru, 562112, Karnataka, India
[b] Biophysical Chemistry Laboratory, Centre for Interdisciplinary Research in Basic Sciences, Jamia Millia Islamia (A Central University), New Delhi, 110025, India
[c] Bio-Organic Division, Bhabha Atomic Research Centre, Trombay, Mumbai, 400 085, India
[d] Department of Biochemistry, Daulat Ram College, University of Delhi, New Delhi, 110007, India

ARTICLE INFO

Keywords:
Oxidovanadium complex
Human lung carcinoma
Human breast adenocarcinoma
Bovine serum albumin
BSA binding
Fluorescence spectroscopy

ABSTRACT

In our ongoing efforts to develop novel trace metal complexes with therapeutically interesting properties, a neutral mono nuclear oxidomethoxidovanadium(V) complex, [$V^{V}O(OCH_3)$(hpdbal-sbdt)] (**1**) and a μ-O bridged dinuclear oxidovanadium(V) complex, [{$V^{V}O$(hpdbal-sbdt)}$_2\mu-O$] (**2**) [H_2hpdbal-sbdt (**I**) is a tridentate and dibasic ONS^{2-} donor ligand obtained through the Schiff base reaction of 2-hydroxy-5-(phenyldiazenyl)benzaldehyde (Hhpdbal) and S-benzyldithiocarbazate (Hsbdt)] have been synthesized and characterized by various analytical techniques such as TGA, EDS, ATR-IR, UV–Vis, CV, ^{1}H NMR, ^{13}C NMR and ^{51}V NMR. Single-crystal X-ray diffraction analysis of **1** confirms the coordination of phenolate oxygen, imine nitrogen and thioenolate sulfur of the ligand to the vanadium center with a distorted tetragonal-pyramidal geometry. The compound **2** triggered apoptotic and reproductive death of the cancer cells *in vitro* with 76% and 62% growth inhibition of human breast adenocarcinoma (MCF-7) and human lung carcinoma cells (A549) respectively. The compound **2** was found to be sufficiently stable over a wide window of physiological pH. The complex **2** was studied further for its interaction with a drug carrier protein BSA with the aid of spectroscopic techniques *viz.* fluorescence, temperature controlled UV–vis and deconvoluted IR techniques.

1. Introduction

Cancer is a global disease burden which causes high level of morbidity and mortality in the context of non-communicable diseases (NCDs). It had an estimated 14 million cases as of 2012 and accounted for about 8.8 million deaths in 2015 [1]. Cases of death due to lung cancer for men and breast cancer for women being the highest, this second leading cause of death worldwide is expected to give a 70% rise in the total number of cases within a span of two decades [2]. In order to combat this deadly ailment, World Health Organization (WHO) had launched a global action plan 2013–2020, which aims for the prevention and control of NCDs according to which designing efficient control strategies for cancer is one of the immediate goals. In this pursuit, countless organic and inorganic compounds have been synthesized for exploring their anticancer activities [3–6]. Notable example of one such compound is cisplatin [7] which is now utilized in the treatment of variety of malignancies [8,9]. Many such platinum based drugs have been developed in the later stages as second generation drugs all of which are limited in their tumor targeting ability and cause undesirable dose-limiting side effects, toxicity [10,11] and drug resistance [10,12] in treated individuals; cisplatin not being an exception. In order to overcome these glitches, extensive research is being done to discover alternative non platinum anticancer drug candidates based on different trace metals with improved pharmacological activities [13]. Vanadium is one among such prospective trace metals which has received huge importance after the discovery of its biological role in certain ascidians and mushrooms [14]. Vanadium has also been recognized as a micronutrient in humans which prevents minor damages occurring to essential biomolecules like DNA and proteins [15]. This directs the attention towards the biological role of vanadium in DNA maintenance and genomic stability thereby preventing mutation of healthy cells leading to cancer [16]. The study of vanadium coordination complexes got further thrust following the exploration of their therapeutic applications [17–22] in terms of antidiabetic, anticancer and antiamoebic activities. Vanadocene compounds [23], amino acid vanadium complexes [24,25], vanadium-oxido [26], vanadium-peroxido [27],

* Corresponding author.
E-mail address: amit.kumar@jainuniversity.ac.in (A. Kumar).

https://doi.org/10.1016/j.jtemb.2018.10.019
Received 11 August 2018; Received in revised form 6 October 2018; Accepted 19 October 2018

polyoxovanadates [28] etc. have shown excellent anticancer and cytotoxic activities on various cancer cells. A Schiff base vitamin B6 derived oxidovanadium complex displayed a remarkable photodynamic therapy effect under visible light targeting the endoplasmic reticulum of HeLa and MCF-7 cancer cells [29]. Curcumin and polypyridyl based vanadium complexes were found to be remarkably cytotoxic in visible light against mouse lymphoma, HeLa, HaCaT and MCF-7 cells [30]. Oxidovanadium complexes have also displayed inhibitory effects over reverse antineoplastic drug resistance [31]. It has been demonstrated that vanadium can inhibit the Epithelial Mesenchymal Transition process which is a key process for migration and colony formation of cancer cells [32]. In the case of MCF-7 and A549 cells in particular, the potent vanadium compound might target the expression of H-Ras Oncogene signal and matrix metalloproteinase-2 signal by intensifying the apoptosis intervened by ROS generation [33,34]. The ligand environment also plays a significant role in the design of bioactive metal complexes; in particular ONS donor Schiff base ligand systems have been found to be of importance due to their applications in various pharmacological activities [35].

The pharmacokinetics of a therapeutic drug candidate with reference to transportation in blood is another critical issue to be addressed. In this direction, a study of metallodrug interaction with serum proteins like BSA and HSA [36] to gauge metallodrug pharmacokinetics and structure-activity relationships [37,38] have attracted a major attention in the scientific fraternity. The study can help in understanding the pharmacodynamics as well and addressing this aspect with the aid of spectroscopic techniques have gained significant importance in the recent days.

In the present study, we describe the synthesis and characterization of mononuclear oxidomethoxidovanadium(V) [$V^{V}O(OCH_3)$(hpdbal-sbdt)] (**1**) and dinuclear oxidovanadium(V) complexes [{$V^{V}O$(hpdbal-sbdt)}$_2\mu-O$] (**2**) (Scheme 1) derived from the ligand benzyl 2-(2-hydroxy-5-(phenyldiazenyl)benzylidene)hydrazinecarbodithioate [H_2hpdbal-sbdt] (**I**).

in vitro antiproliferative and apoptosis-inducing activities against MCF-7 (human breast adenocarcinoma) and A549 (human lung carcinoma) cells were established for ligand **I** and complex **2**. Furthermore, interaction of **I** and **2** with BSA were studied to provide insight into the nature of binding and the thermodynamic parameters *viz.* ΔG, ΔH and ΔS involved in the protein binding process.

2. Experimental

2.1. Materials

All solvents and chemicals procured for the experiments were used as received. Aniline, salicylaldehyde, hydrazine hydrate monohydrate, carbon disulphide, benzyl chloride, vanadium pentoxide and triethylamine (anhydrous) were obtained from Spectrochem Pvt. Ltd. Sodium nitrite and sodium chloride were procured from Fischer Scientific. Sodium carbonate (anhydrous), sodium hydroxide and KOH pellets were procured from Himedia. Acetyl acetone and hydrochloric acid were obtained from Merck and S D Fine-Chem Ltd. respectively. AR grade solvents and doubly distilled water were used throughout the experiments. [$VO(acac)_2$] was prepared following a reported method [39]. 2-Hydroxy-5-(phenyldiazenyl)benzaldehyde (Hhpdbal) and S-benzyl dithiocarbazate (Hsbdt) were synthesized according to reported literature [40]. The ligand [H_2hpdbal-sbdt] (**I**) was prepared in accordance with our previously reported work [41] (see section SI-1 and scheme SI-1). Synthesis of vanadium complexes [$V^{V}O(OCH_3)$(hpdbal-sbdt)] (**1**) and [{$V^{V}O$(hpdbal-sbdt)}$_2\mu-O$] (**2**) in detail is outlined in sections 2.6.1 and 2.6.2 respectively.

2.2. Instrumentation

^{1}H and ^{13}C-NMR spectra were recorded with Agilent 400MR DD2 FT-NMR Spectrometer using $SiMe_4$ as an internal standard. ^{51}V NMR spectra were obtained on a Varian-Mercury Plus 300 MHz NMR spectrometer in DMSO-d_6. Elemental analysis was carried out using Euro Vector E-3000 system. UV–vis spectra were measured using a UV-1800 Shimadzu UV–vis Spectrophotometer. ATR-IR spectra of solid compounds were obtained from Bruker Alpha Single reflection ATR module equipped with ZnSe crystal. Energy Dispersive X-ray Spectroscopic (EDS) analysis were acquired from JEOL-JSM7100F. The sample for EDS was coated with a thin layer (6–8 nm) of platinum by sputtering method using a JEC-3000FC auto fine coater for about 100 s. TGA analysis was performed on a Perkin Elmer STA 6000TG/DTA analyzer up to 700 °C. The cyclic voltammograms were recorded using a PC-controlled CHI660D potentiostat (CH Instruments, Austin, USA) under nitrogen atmosphere and room temperature. Measurements were made using a three compartment cell consisting of glassy carbon as working, platinum-wire as auxiliary and silver wire as reference electrodes. Potentials were referred to AgCl/Ag using the ferrocene/ferrocenium couple ($Fe(\eta^5\text{-}C_5H_5)_2]^{0/+}$, $E^{red}_{1/2}$ $E_{1/2}$ = 0.549 V) as an internal standard with a scan rate of 0.1 V/s. A pH meter (HI5000 Series, Hanna) calibrated with standard buffers of pH 4 and 7 was used for determining pKa.

2.3. Crystal structure determination

Single crystal of compound **1** was mounted on a Microstar Proteum 8 Bruker Smart Apex CCD diffractometer equipped with graphite monochromator and CuK_α radiation (λ = 1.54178 Å) to obtain the diffraction data. The crystallographic data and refinement details are given in Table 1. The unit cell dimensions and intensity data were measured at 296 K. The intensity data were corrected for Lorentz polarization absorption effects. Absorption corrections were done using SADABS program. The structure was solved by direct methods using the

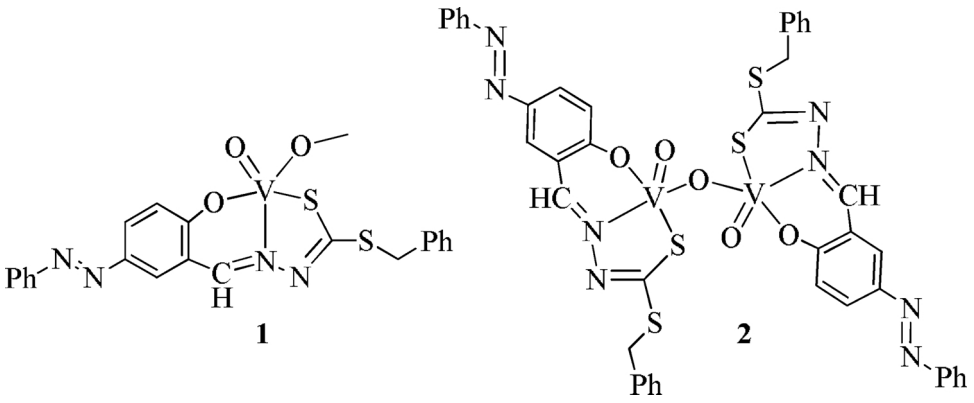

Scheme 1. Oxidovanadium complexes [$V^{V}O(OCH_3)$(hpdbal-sbdt)] (**1**) and [{$V^{V}O$(hpdbal-sbdt)}$_2\mu-O$] (**2**) obtained in this study.

Table 1
Crystal data and refinement details for [$V^{V}O(OCH_3)$(hpdbal-sbdt)] **(1)**.

empirical formula[a]	$C_{22}H_{19}N_4O_3S_2V$	Density (calc.), g cm^{-3}	1.530
fw[a], g mol^{-1}	502.47	absorption coefficient, mm^{-1}	5.875
wavelength (Å)	1.54178	F(000)	516
cryst syst	triclinic	crystal size, mm^3	0.29 × 0.26 × 0.22
space group	P-1	θ range for data collection, deg	5.77-64.37
unit cell dimensions:		index ranges	−8≤ h ≥ 8 −8 ≤ k ≥ 7 −26 ≤ k ≥ 27
a, Å	7.0323	reflns collected	12750
b, Å	7.1209	independent reflns	3607 [R (int) = 0.0520]
c, Å	23.2372(7)	completeness to θ (max), %	98.5
α, deg	97.547	data/restraints/params	3607/0/290
β, deg	90.160	GOF on F^2	1.035
γ, deg	108.833	final R indices [I > 2σ(I_0)]	R1 = 0.0437,wR2 = 0.1331
volume, $Å^3$	1090.53	R indices (all data)	R1 = 0.0451,wR2 = 0.1352
Z	2	largest diff. peak/hole, e$Å^{-3}$	0.580/ –0.433

[a] per formula weight.

program SHELXS-90 and refined using least squares with the SHELXL-97 program. H atoms were either placed or found in calculated positions and isotropically refined using a riding model. Anisotropic refinement was applied for the non-H atoms.

2.4. Preparation of BSA solution

BSA (fatty acid free) solution was prepared by dissolving it in sodium phosphate buffer of pH 7.4 (see section SI-2). UV spectrophotometric method was used to estimate the concentration of the solution knowing the extinction coefficient of BSA (43,890 M^{-1} cm^{-1} at 280 nm) [38b]. Following this, BSA stock solution (5μM) and stock solutions of ligand [H_2hpdbal-sbdt] (**I**) and [{$V^{V}O$(hpdbal-sbdt)}$_2\mu-O$] (**2**) were prepared in pH 7.4 buffer and DMSO respectively. Thermodynamic studies were conducted using a temperature controlled Analytik Jena Specord-250 spectrophotometer. Quenching studies were performed using a Varian Cary Eclipse spectrofluorometer equipped with a 150 W xenon lamp. BSA conformational studies were carried out using a Specac Golden Gate diamond ATR sampler fitted to a Bruker Tensor 27 with an MCT detector.

2.5. Anticancer activity

The anticancer activities of [{$V^{V}O$(hpdbal-sbdt)}$_2\mu-O$] (**2**) and ligand H_2hpdbal-sbdt (**I**) were evaluated by employing two different cell lines MCF-7 (human breast adenocarcinoma) and A549 (human lung carcinoma). A vehicle control (1% DMSO) was included in all the experiments. Antiproliferative/anticancer activities were evaluated by microscopic observation of morphological changes, MTT assay, clonogenic assay and quantification of apoptosis by subG1 population. For observation of morphological changes, 0.1 × 10^6 cells/well were plated in 6 well plates in 2 mL DMEM medium and treated with 25 μM each of the test compounds for 24 h and then observed in microscope for any changes. Similar procedure was followed for apoptosis detection and quantification where after treatment and incubation for 24 h, the cells were collected by trypsinization and stained (PI 50 μg/mL, Na-citrate 0.1% and triton X 100 0.1% and RNAse 50 μg/mL). The samples were acquired in a flow cytometer and the extent of apoptosis in each sample was quantified. For MTT assay, 10,000 cells were plated per well in a 96 well plate and the cells were allowed to attach overnight. The compounds (25 μM) were added and incubated for 48 h followed by removal of media by gentle aspiration. The wells were then filled with 0.2 mL MTT (0.5 mg/mL in phosphate buffered saline) and incubated for 4 h. At the end of incubation, the insoluble product formed was solubilized by 0.2 mL of solubilization buffer (10% SDS in 0.01 N HCl) per well. The readings were read using a microplate reader at 550 nm. The percentage inhibition was plotted in comparison to vehicle treated cells. For clonogenic assay, 750 cells were plated in a 6 well plate and allowed to attach overnight. The compounds (25 μM) were then added and incubated for 10 days followed by fixing of cells with chilled methanol and staining with 0.5% crystal violet for visual observation of reproductive cell death.

2.6. Synthesis

2.6.1. Synthesis of [$V^{V}O(OCH_3)$(hpdbal-sbdt)] (1)

[$V^{IV}O$(acac)$_2$] (0.56 g, 2.1 mmol) was taken in 20 mL of methanol and to this was added a solution of H_2hpdbal-sbdt (**I**) (0.80 g, 2.0 mmol) dissolved in 20 mL of DCM. The reaction mixture was refluxed for 30 min followed by aerial oxidation. The formation of complex **1** was triggered by the addition of 3 drops of triethylamine as a mild base during reflux. Keeping the filtrate from the above reaction for ca. 24 h gave brown color X-ray quality crystals of **1**. Yield: 60%; Anal. Calcd. for $C_{22}H_{19}N_4O_3S_2V$(MW: 502.47): C, 52.59; H, 3.81; N, 11.15; S, 12.76. Found: C, 52.61; H, 3.65; N, 11.21; S, 12.62. Selected ATR-IR data (ν/cm^{-1}): 1602 (C = N), 1472, 1571 (N = N), 1101 (C–O), 760 (C–S), 1369 (C–N), 3034 (aromatic C–H), 968 (V = O); ^{1}H-NMR (400 MHz, DMSO-d_6): δ8.29-7.15 (m, 13H, aromatic H), 8.86 (s, 1H, N = CH), 4.45 (s, 2H, S-CH_2), 2.75 (s, 3H, O-CH_3); ^{13}C–NMR (400 MHz,DMSO-d_6): δ118.15 (C-1), 165.85(C-2), 117.88 (C-3), 126.52(C-4), 145.13(C-5), 122.71(C-6, C-8, C-12), 152.65(C-7), 129.04(C-9, C-11), 131.13(C-10), 148.98(C-13), 204.65(C-14), 46.25(C-15), 136.55(C-16), 128.67(C-17, C-21), 128.82(C-18, C-20), 126.29(C-19), 69.42 (C-22, –OCH_3);^{51}V NMR (DMSO-d_6, δ ppm): –468.5.

2.6.2. Synthesis of [{$V^{V}O$(hpdbal-sbdt)}$_2\mu$-O] (2)

Solution of **1** (0.41 g, 1 mmol) in 20 mL of methanol was refluxed on a water bath for 2 h which resulted in the separation of a green solid. Upon cooling the solution to room temperature, the product was filtered, isolated, washed with methanol and dried *in vacuo* over silica gel. Yield: 85%; Anal. Calcd. For $C_{42}H_{32}N_8O_5S_4V_2$ (MW: 958.90): C, 52.61; H, 3.36; N, 11.69; S, 13.38; Found: C, 52.69 ; H, 3.39; N, 11.75; S, 13.47; Selected ATR-IR (ν/cm^{-1}): 1591 (C = N), 755 (C–S), 1350 (C–N), 1102 (C–O), 1455, 1535 (N = N), 2982 (aromatic C–H), 956 (V = O), 827 (V–O–V); ^{1}H-NMR (400 MHz, DMSO-d_6): δ8.37–7.26 (m, 26H, aromatic H), 8.81 (s, 2H, N = CH), 4.44 (s, 4H, S-CH_2); ^{13}C–NMR (400 MHz, DMSO-d_6): δ118.13 (C-1, C-22), 164.35(C-2, C-23), 117.82 (C-3, C-24), 126.54(C-4, C-25), 144.89(C-5, C-26), 122.51(C-6, C-8, C-12, C-27, C-29, C-33), 152.82(C-7, C-28), 128.99(C-9, C-11, C-30, C-32), 130.95(C-10, C-31), 148.33(C-13, C-34), 204.72(C-14, C-35), 46.28(C-15, C-36), 136.55(C-16, C-37), 128.78(C-17, C-21, C-38, C-42), 128.98(C-18, C-20, C-39, C-41), 126.35(C-19, C-40); ^{51}V NMR (DMSO-d_6, δ ppm): –465.2.

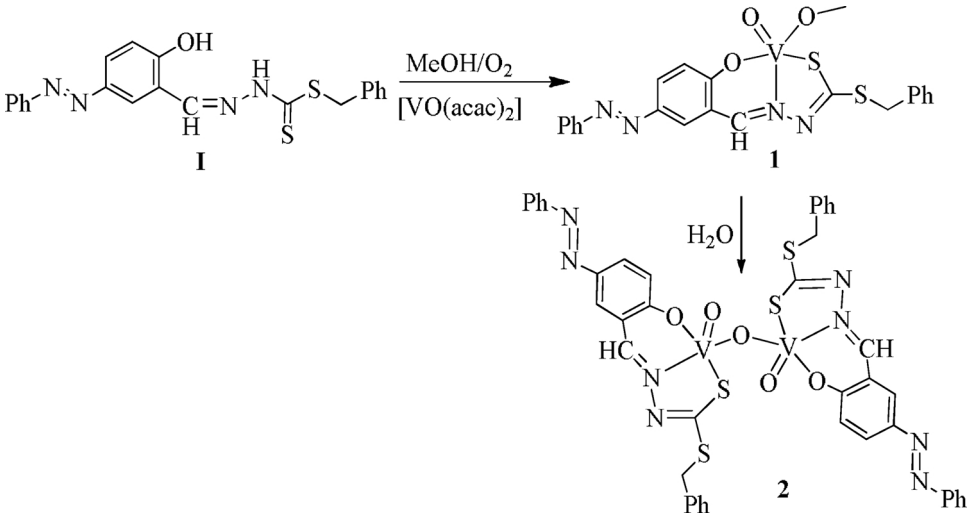

Scheme 2. Synthesis of $[V^{V}O(OCH_3)(hpdbal\text{-}sbdt)]$ and $[\{V^{V}O(hpdbal\text{-}sbdt)\}_2\mu\text{-}O]$.

3. Results and discussion

The reaction between equimolar solutions of $[V^{IV}O(acac)_2]$ in methanol and H_2hpdbal-sbdt (**I**) in DCM in the presence of triethylamine yielded the $V^{V}O$-complex $[V^{V}O(OCH_3)(hpdbal\text{-}sbdt)]$ (Eq. (1) and Eq. (2)) The reaction of $[V^{V}O(OCH_3)(hpdbal\text{-}sbdt)]$ in solution leads to transformation into the corresponding μ-O bridged dinuclear oxidovanadium(V) complex $[\{V^{V}O(hpdbal\text{-}sbdt)\}_2\mu\text{-}O]$ (Eq. (3)).

$$[V^{IV}O(acac)_2] + H_2hpdbal\text{-}sbdt \rightarrow [V^{IV}O(hpdbal\text{-}sbdt)] + 2Hacac \quad (1)$$

$$2[V^{IV}O(hpdbal\text{-}sbdt)] + 2MeOH + \tfrac{1}{2}O_2 \rightarrow 2[V^{V}O(OCH_3)(hpdbal\text{-}sbdt)] + H_2O \quad (2)$$

$$2[V^{V}O(OCH_3)(hpdbal\text{-}sbdt)] + H_2O \leftrightarrows [\{V^{V}O(hpdbal\text{-}sbdt)\}_2\mu\text{-}O] + 2MeOH \quad (3)$$

The structural formulae were deduced based on elemental analysis, spectroscopic techniques and single crystal X-ray diffraction analysis of compound **1**. Scheme 2 provides an overview of how the complexes described in this work were obtained.

3.1. Characterization of compounds

3.1.1. Structure description

ORTEP plot of oxidomethoxidovanadium(V) complex **1** is depicted in Fig. 1. The complex crystallised with a $-OCH_3$ group from the solvent methanol as a donor monodentate ligand per formula unit. The five-coordinated vanadium complex exhibited a slightly distorted tetragonal-pyramidal coordination geometry with the doubly bonded oxygen atom in the apex, the τ value being 0.12 (τ = 0 for an ideal square pyramid, τ = 1 for an ideal trigonal bipyramid) [42]. The distortion is significantly lower than in the related thiohydrazonato complexes such as [VO(OEt)(sal-sbdt)] (H_2sal-sbdt = Schiff base derived from salicylaldehyde and *S*-benzyldithiocarbazate; τ = 0.27) and $[VO_2(acpy\text{-}sbdt)]$ (Hacpy = Schiff base derived from acetylpyridine and *S*-benzyldithiocarbazate; τ = 0.47) but very similar to $[VO_2(Hpydx\text{-}sbdt)]$ (Hpydx = Schiff base derived from pyridoxal and *S*-benzyldithiocarbazate; τ = 0.13) [18–20,43].

The basal plane is made up by the O-phenolato, S-enolato and N-imine atoms from the ligand and oxygen atom from the methoxide group. The Schiff base ligand forms a six-membered ring of S—V—N with an angle of 77.66 and a five membered chelate ring of O—V—N with an angle of 92.37. (Table SI-1) The V=O bond (V—O(2)) length of 1.588 Å is characteristic of a strong π bonding between the vanadium center and the oxido oxygen. Consequently, there is no deviation in the bond length as the normal V=O bonds in other oxidovanadium complexes commonly range from 1.57 to 1.62 Å. Strong parallel π-π interactions were found between the parallel phenyl rings of the sbdt backbone and the parallel phenyl rings of the aldehyde backbone in the two neighboring complex molecules with the centroid distances of 3.924 Å and 3.645 Å respectively (Figure SI-1). Hence the supramolecular structure of **1** is greatly stabilised by π- π interactions between the phenyl rings.

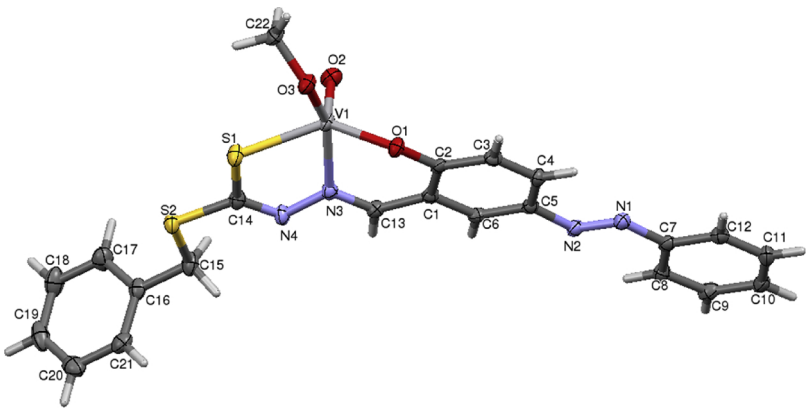

Fig. 1. ORTEP diagram of $[V^{V}O(OCH_3)(hpdbal\text{-}sbdt)]$ **(1)**.

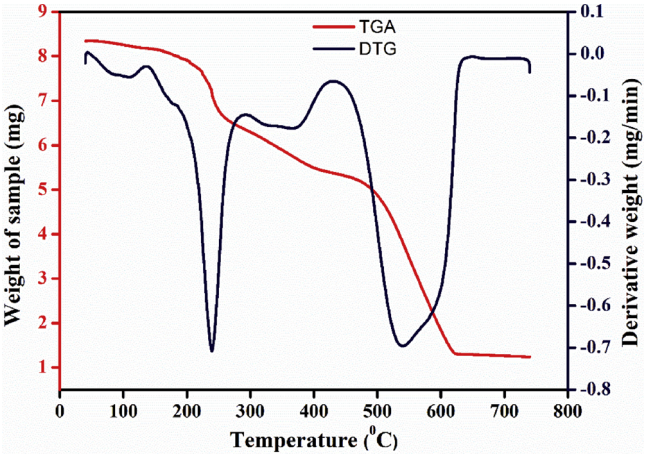

Fig. 2. TGA-DTG profile of [{V^{V}O(hpdbal-sbdt)}$_2$μ-O] obtained from thermal analysis at a temperature range of 40–750 °C.

3.1.2. Thermogravimetric analysis (TGA) and energy dispersive spectroscopic (EDS) analysis

TGA and EDS analysis were performed for [{V^{V}O(hpdbal-sbdt)}$_2$μ-O] (**2**) as single crystals of x-ray diffraction quality were not obtained. The TGA analysis and the derivative thermogram (DTG) profile of the dinuclear complex [{V^{V}O(hpdbal-sbdt)}$_2$μ-O] (Fig. 2) gave a definitive evidence of the predicted structure of **2**. The thermal analysis was carried out in a temperature range of 40–750 °C with a heating rate of 20 °C/min under dynamic air atmosphere. The sample showed 2.03% weight loss in the range of 60–145 °C corresponding to the loss of bridging oxygen (-O-, calc. 1.67%) [18]. The subsequent weight loss of 25.89% corresponds to the elimination of 2 units of –$SCH_2C_6H_5$ of the sbdt ligand backbone between 145–330 °C ($C_{14}H_{14}S_2$, calc. 26.16%). This was followed by the loss of 2 units of –SCN in the range of 330–483 °C corresponding to the loss of 15.98% weight ($S_2C_2N_2$, calc. 16.70%). The final and major weight loss of 71.57% occurred between 483–620 °C which can be related to the elimination of 2 azo linked oxygen donor backbone units with one oxygen atom still intact with the vanadium metal center [$(C_{13}H_9N_2)_2O$, calc. 69.45%]. Overall, the total weight loss of 82.65% tallied with the total organic content decomposition in the sample minus one oxygen atom approximately (calc. 81.52). Accordingly, the residual weight of 17.35% matched to vanadium pentoxide and this value is very close to the theoretically calculated value of the oxide material left (V_2O_5, calc. 18.48%) (Table SI-2).

EDS analysis further confirmed the presence of the predicted metal center in [{V^{V}O(hpdbal-sbdt)}$_2$μ-O] (**2**) which was not observed in the case of ligand and this confirmed the incorporation of vanadium ion in the ligand. The absence of external impurities in the samples was confirmed through the EDS spectra (Figs. 3a and 3b). Peaks observed for platinum are due to the coating of platinum to the samples during EDS sampling for attaining conductive surface.

3.1.3. ATR-IR spectral study

Characteristic IR vibrations of the important functional groups were studied (Figures SI-2, SI-3 and SI-4). The ligand exhibited a strong band at 1032 cm^{-1} due to the C═S group which justifies the thiocarbonyl nature. The N—H stretching due to the hydrazide part of the ligand was observed as a sharp peak at 3100 cm^{-1}. The absence of N—H band in the spectra of complexes can be attributed to the coordination of the enethiolato sulphur to the vanadium center. This observation is due to the probable conversion of thioamide form of the ligand to the imidothiol. The band for C—S stretch was observed in the range of 771–755 cm^{-1} for both ligand and metal complexes. Coordination of the imine nitrogen to the metal centers is explained by a bathochromic shift of the C═N stretching (1607 cm^{-1}) of the ligand system by 5–16 cm^{-1}. The band for para substituted azobenzene (Ph–N = N–) was found in two regions [44] *viz.* 1455–1483 cm^{-1} and 1518–1571 cm^{-1}. C—N stretching was found in the region of 1320–1377 cm^{-1} for the samples with slight variations in the complexes. An average intense band varying between 1102 and 1117 $cm^{-1}$was observed due to the phenolic C—O stretching. C—H stretching from monosubstituted benzene, p-substituted benzene and imine carbon were noticed between 682–692 cm^{-1}, 823–829 cm^{-1} and 2857–3048 cm^{-1} respectively. Sharp bands at 968 cm^{-1} and 956 cm^{-1} are due to the V═O stretching modes in complex **1** and **2** respectively and the vibrational peak at 827 cm^{-1} is attributed to the V–*μ*—O–V stretching in complex **2**.

3.1.4. ^{1}H, ^{13}C and ^{51}V NMR spectra

^{1}H NMR spectra of the ligand and complexes were recorded in DMSO-d_6 to confirm the coordinating modes. The signal for phenolic proton observed at 13.23 ppm for the ligand vanished in the NMR spectra of metal complexes which is attributable to the coordination of the phenolic oxygen to the vanadium center by the loss of a proton. A new resonance at 2.75 ppm appeared in the spectrum of species **1** due to the –OCH_3 linkage. The resonance for NH/SH vanished in both complexes which is due to the coordination of the thioenolate sulphur to the metal centers. Notable downfield shifts were observed in the complexes for the azomethine proton on account of imino nitrogen coordination. The proton signals of metal species **2** exhibited relatively broad signals which can be attributed to the dinuclear centre/dimeric nature [19], molecular aggregations or internal flexibility [45]. Residual proton signals pertaining to the ligand backbone did not shift and appeared in the expected range following complexation. It was hence found that ^{1}H NMR spectra is in full agreement with the tridentate

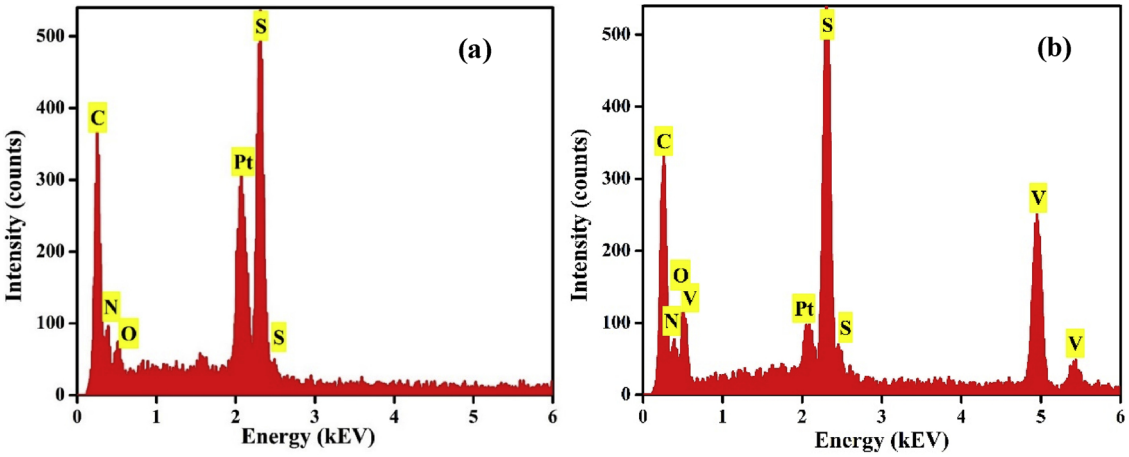

Fig. 3. EDS spectra of **(a)** H_2hpdbal-sbdt (**I**) and **(b)** [{V^{V}O(hpdbal-sbdt)}$_2$μ-O] **(2)**.

Table 2
Electronic spectral data and electrochemical data of the compounds.

Compounds	λ_{max} (nm)	Molar absorption coefficient ε (L mol^{-1} cm^{-1})	E_{pc} (V)	E_{pa} (V)	E° (V)
I	208	760000	–	–	–
	340	42000			
1	207	640000	–0.128	–0.080	–0.104
	345	22000			
	468	6000			
2	207	666000	–0.131	–0.079	–0.105
	344	26600			
	470	2900			

ONS^{2-} coordination behavior of the ligand in the complexes.

To additionally support this coordination mode, ^{13}C NMR spectra of the complexes were compared with the ^{13}C NMR spectrum of the ligand. The complexes **1** and **2** resonated in the similar range as that of the ligand except with a considerable downfield shift Δδ (0.8–8.7 ppm) for carbon atoms bonded to the donor O, N and S atoms. Also, in complex **1**, a new signal appeared at 69.42 ppm owing to the carbon atom of the coordinated methoxy group.

The complexes $[V^{V}O(OCH_3)$(hpdbal-sbdt)] and $[\{V^{V}O$(hpdbal-sbdt)$\}_2\mu$-O] were also characterized in solution by recording ^{51}V NMR in DMSO-d_6 using ammonium vanadate (NH_4VO_3) (δ ppm = –576) as an external standard. The δ value exhibited a strong broad resonance at –468.5 ppm and –465.2 ppm for **1** and **2** respectively which confirms the participation of the soft S atom, O and N donor atoms in coordinating to the vanadium center [46]. The methoxy linked complex **1** resonated in a comparatively downfield region as the coordination of methoxy to the V^{V} center increases the shielding of metal thereby causing resonance to shift further in the negative region [47].

3.1.5. Electronic spectral study and electrochemical study

UV-Vis spectra of **I**, **1** and **2** were recorded in DMSO (Table 2). Ligand **I** exhibited two absorption peaks at 208 nm and 340 nm which are preferably allotted to the π- π* and n- π* transitions [48] respectively. The complexes showed absorption peaks at 207 nm and 345 nm for **1** and 207 nm and 344 nm for **2** along with an added low absorbance band at 468 nm and 470 nm respectively due to the ligand-to-metal charge transfer phenomenon from the phenolate oxygen to an empty d orbital of the vanadium ion.

For the cyclic voltammetric measurements, 1 mM solution of the complexes **1** and **2** in anhydrous DMSO was prepared for testing along with 0.1 M of tetrabutylammonium hexafluorophosphate (Bu_4NPF_6) in acetonitrile as the supporting electrolyte. Ferrocene (1 mM) solution in the electrolyte was used as the standard reference. The redox behaviors of the compounds **1** and **2** were obtained from the cyclic voltammograms recorded with a potential scan range of –0.5 V to 0.2 V. Both reduction and oxidation peaks were found to be sharp. The observed standard reduction potential (E°) and the smaller peak-to-peak separation directed attention to the facile one electron quasi reversible reduction-oxidation couple of V(V)↔V(IV) species [22]. The cathodic peak potential indicating reduction (E_{pc}) and anodic peak potential indicating oxidation (E_{pa}) along with E° values for **1** and **2** are mentioned in Table 2.

3.2. Anticancer studies

The anticancer property of the ligand **I** and the metal complex **2** were investigated by evaluating their activity against MCF-7 (human breast adenocarcinoma) and A549 (human lung carcinoma) cell lines using 1% v/v DMSO as a solvent. A standard concentration of 25 μM was fixed as the optimum concentration of the test compounds citing best results at this concentration during optimization studies. The untreated cancer cells were considered as control and cells treated with 1% DMSO were considered as vehicle or negative control. Complex **1** was not studied as it was found to be unstable in solution state when kept for prolonged durations and got converted into the dimeric species.

3.2.1. Microscopic observation to detect cellular morphological changes

Upon individual treatment of the breast cancer and lung cancer cells with 25μM of each sample for 24 h, marked morphological changes were observed under a microscope in the breast cancer and lung cancer cells incubated with ligand **I** and in the lung cancer cells incubated with the complex **2** (Fig. 4a and b). Particularly, in the case of A549 cells treated with $[\{V^{V}O$(hpdbal-sbdt)$\}_2\mu$-O] (**2**), cell shrinkage and release of apoptotic like bodies were observed which is an evidence of cancer cell death induction.

3.2.2. MTT assay to quantify antiproliferative activity

The antiproliferative activity was evaluated by incubation of cell lines with 25 μM final concentration of each compound for 48 h

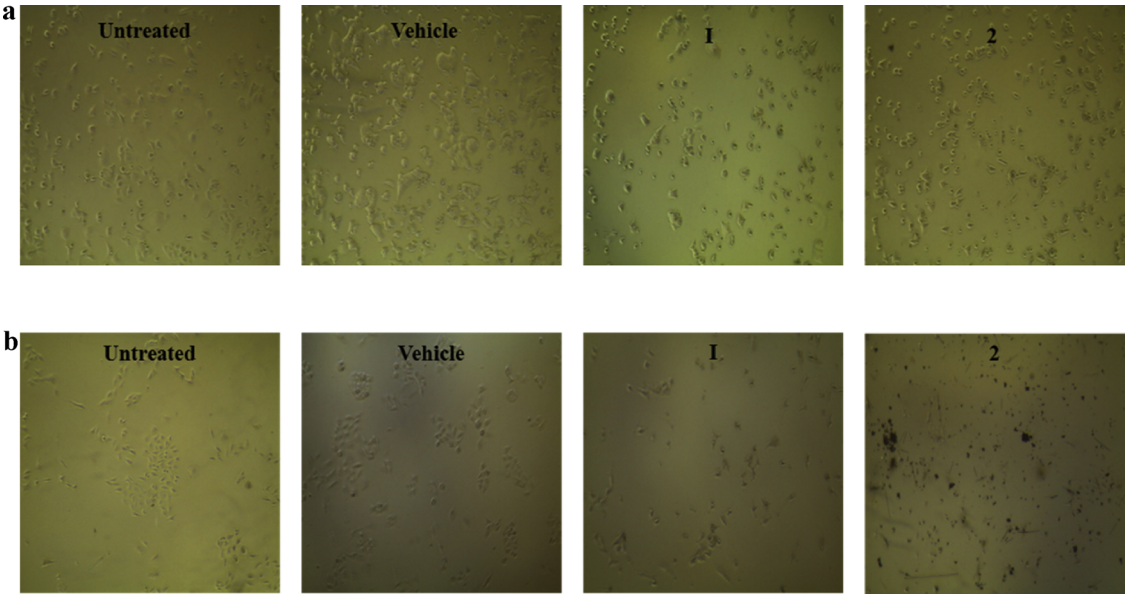

Fig. 4. (a) MCF-7 cells observed after 24 h incubation. (b) A549 cells observed after 24 h incubation.

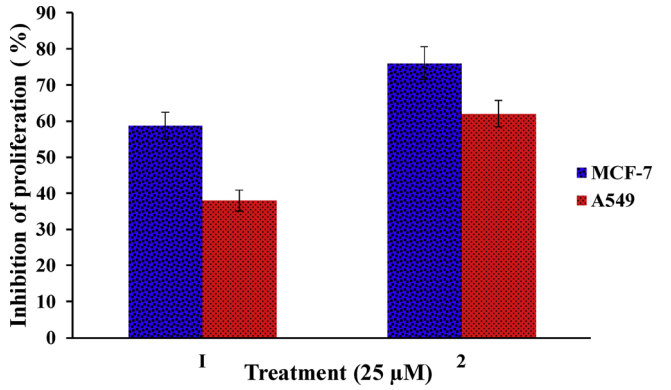

Fig. 5. Graphical representation of MTT assay which quantifies proliferation inhibition of cancer cells.

followed by staining and incubation with MTT, a yellow tetrazole dye for 4 h. If proliferation of cancer cells are hindered, lesser of the MTT dye gets reduced to purple formazan which thereby decreases the fluorescence given by the respective cell line as compared to the control cell. From the fluorescence readings taken at 550 nm, it can be deduced that the complex **2** exhibits significant antiproliferative activity with about 76% and 62% inhibition against MCF-7 and A549 cells respectively. The ligand showed moderate and poor activity against MCF-7 and A549 cells respectively (Fig. 5).

3.2.3. subG1 analysis for apoptosis detection and quantification

Induction of apoptosis in cancer cells treated with test compounds was quantified using a flow cytometer. For this, 25 µM of the compounds incubated with the cell lines for 24 h in assay were collected by trypsinization, stained and acquired in a flow cytometer. SubG1 population was quantified that indicated the presence and extent of apoptosis (Fig. 6a and b). Substantial apoptosis was observed in both cell lines treated with the test compounds. Apoptosis was found to be highly significant in the case of A549 cells incubated with the dimeric vanadium complex **2** which has about 97.5% of cell population in the subG1 phase and is a characteristic of apoptotic cells.

3.2.4. Clonogenic assay for visual quantification of reproductive cell death

Clonogenic assay, also termed as colony formation assay, is an *in vitro* cell survival assay which is based on the capability of a single cell to cultivate into a colony. This assay is indicative of the extent of reproductive death of the cells following long-term treatment with drug candidates. The cancer cells were treated with 25 µM each of test compounds and incubated for 10 days. The death of cells was visualized after fixing the treated cells with chilled methanol followed by staining with crystal violet dye. The percentage of cells that survived were almost nil and complete absence of cloned cells was observed in treated samples (Fig. 7a and b).

All the assays indicated that the complex **2** is a potent anticancer agent and the activity shown was comparable with previously known standard drugs like cisplatin which showed 58% and about 60% reduction of cell viability when treated against MCF-7 cells [49] and A549 cells [50] respectively for 24 h. The IC_{50} value of cisplatin was found to be 28 ± 6.0 µM against growth of MCF-7 cells [51] and in this case, the dimeric vanadium complex **2** has exhibited higher growth inhibition properties at a concentration of 25 µM.

In the present case, various mechanistic approaches can be postulated to justify the cytotoxic activity of the vanadium complex against the tumor cells. One possibility is the depolarisation of the mitochondrial membrane of the cancer cells by the arrest of G0/G1 phase of cell division which leads to the activation of capsase-12 [52] and thereby causing apoptosis induced by ER stress. Another likely perspective being apoptosis induction by DNA fragmentation and Anoikis-related apoptosis by vanadium [53].

3.3. pH stability studies

The optimum physiological pH is 7.4 for humans and hence stability study of the compounds in aqueous media under this pH range is crucial to understand if the compound itself is an active species for exhibiting anticancer activity or it undergoes any disintegration or transformation to give another active species. Potentiometric titration and UV–vis titration studies with different pH conditions were carried out for the bioactive compound **2** in order to test their solution stability. The physicochemical properties of drugs are highly influenced by their pK_a values and hence the pK_a value of the anticancer compound **2** was assessed by titrating it with varied pH conditions using a pH meter [54,55]. The solution of the compound **2** (0.5 mM) was prepared in 90% (v/v) of water/DMSO mixture. The pH of the compound in this solution was about 5.0 and this pH was gradually brought down to pH 3 by titrating with HCl (5 mM). Following this, the trend in pH variation was studied with the slow addition of KOH (5 mM) solution from pH 3 to 9 and from the plot of pH vs volume of KOH added, (Figure SI-5) pKa of the compound **2** was found to be 6.22.

UV-Visible spectral studies were also carried out at different pH conditions (3–9) to test the stability of **2** under physiological conditions. With HCl addition, a slight reduction in absorption intensity of the major peak at 344 nm was seen with no new absorption peaks detected (Figure SI-6a). A reverse trend was observed with the slow addition of KOH solution until pH 9 i.e. a marginal increase in absorbance intensity was seen with increasing pH and no extra peaks were detected (Figure SI-6b). The original absorbance band was intact at both acidic and basic pH range which illustrates that the compound **2** is stable over a wide pH range of 3–9. The intensity shifts observed are purely caused by the equilibrium shift between the deprotonated and protonated forms of **2**.

It is proposed that on treatment with HCl, the hydrazone nitrogen of the dioxo complex gets protonated [56,57] and with the increase in pH upon addition of KOH, the hydrazone nitrogen gets deprotonated. The pK_a value and the reversibility trend witnessed in UV spectra suggest that there is an equilibrium at pH 6.22 between the deprotonated and protonated species [58] and hence at physiological pH of 7.4, the compound **2** will mostly be in the deprotonated state or in its native form. The compound can hence be stipulated to remain stable under different pH environment prevailing in the human body.

3.4. BSA interaction studies

BSA, a model serum protein behaves as a major reservoir of drug molecules thereby affecting the overall bioavailability of a particular drug. Thus, a study of the binding behavior between BSA and bioactive drug-like compounds is of momentous importance. The ligand **I** and the active vanadium complex **2** were studied for their interaction with BSA using multi-spectroscopic methods.

3.4.1. Steady state/Intrinsic fluorescence study

Fluorescence spectroscopy is a versatile tool to obtain the type of quenching mechanism, binding constant and the number of binding sites involved in the binding reaction between BSA and the compound [59]. Fluorescence emission spectra of BSA (5µM) upon titration with ten different concentrations (0.83 µM to 8.26 µM each) of the ligand (**I**) and complex (**2**) solutions in phosphate buffer of pH 7.4 at 298 K were obtained by fixing excitation wavelength at 280 nm (Figs. 8a and 8b). BSA showed emission maxima at around 347 nm and with the addition of the compounds, the peak got gradually quenched. The quenching pattern induced by the compounds might be due to different molecular interactions like energy transfer, excited state reactions, molecular rearrangements, ground-state complex formation or collisional quenching. To evaluate which one of them is in action in the present case, Stern-Volmer equation [60] (eq. 4) was used as a standard

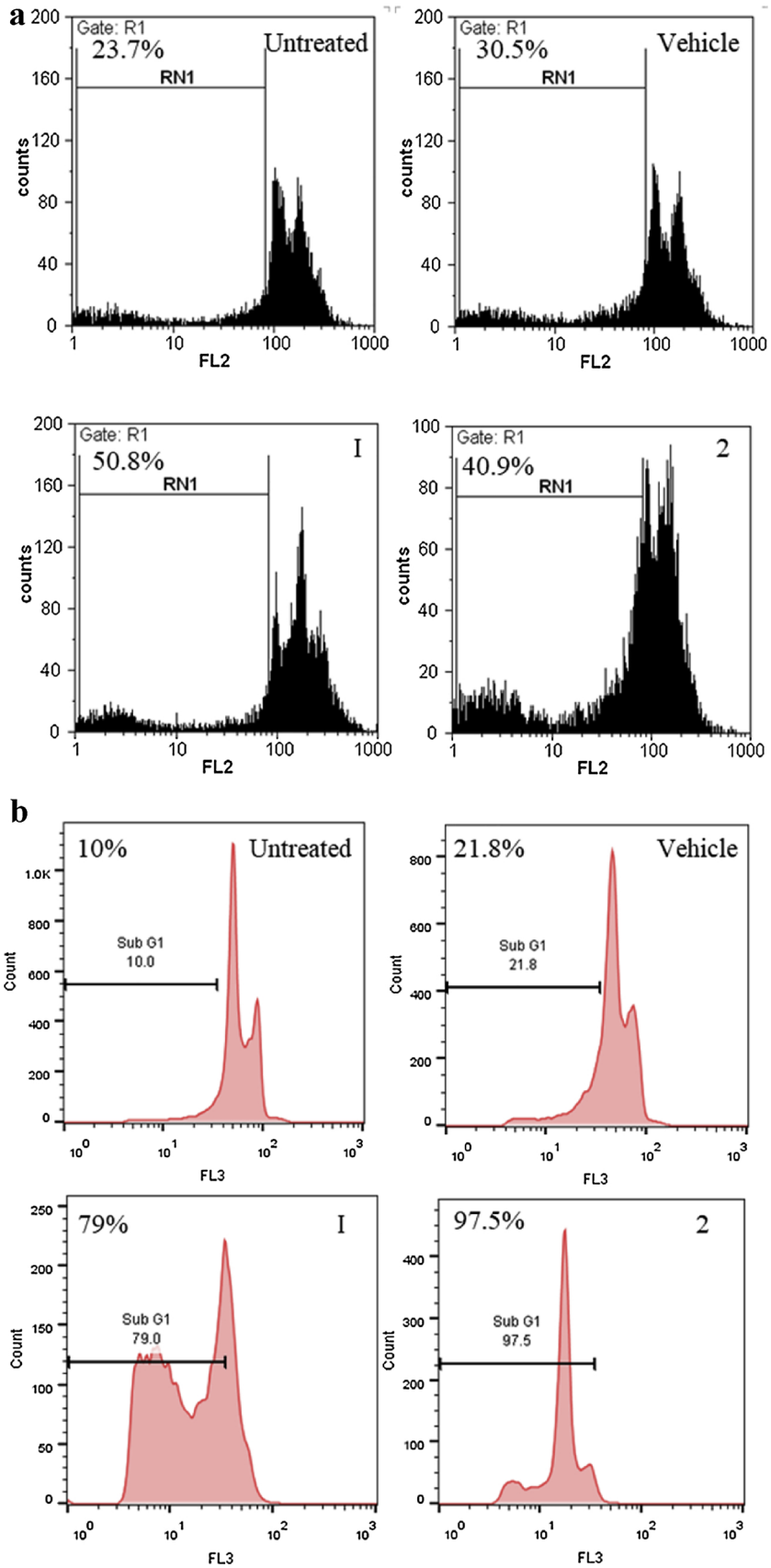

Fig. 6. (a) Flow cytometric analysis of subG1 population in MCF-7 cells after treatment with test compounds. (b) Flow cytometric analysis of subG1 population in A549 cells after treatment with test compounds.

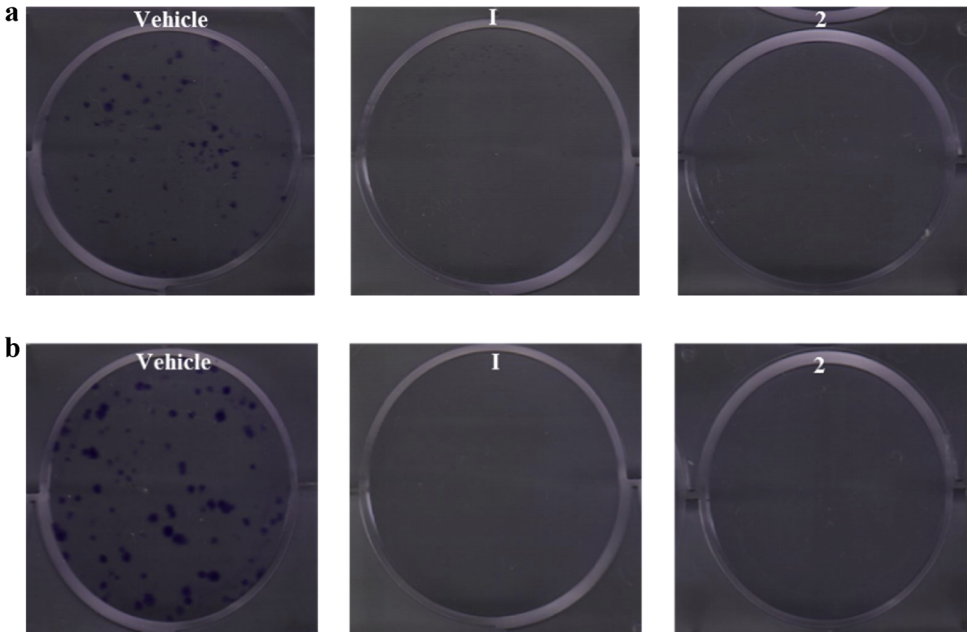

Fig. 7. (a) Clonogenic assay of vehicle treated and test sample treated MCF-7 cells stained with crystal violet after 10 days. (b) Clonogenic assay of vehicle treated and test sample treated A549 cells stained with crystal violet after 10 days.

equation as given in eq. 4

$$\frac{F_0}{F} = 1 + k_q \tau_0 [Q] = 1 + K_{SV}[Q] \quad (4)$$

where F_0 is the fluorescence peak intensity of pure BSA and F is the fluorescence peak intensity of BSA added with various concentrations of the quencher compound. k_q is the quenching rate constant of the biomolecular reaction and K_{sv} is the Stern-Volmer quenching constant. [Q] and τ_0 refer to the concentration of the compound and the average lifetime of the pure BSA molecules (10^{-9} s) respectively. For both BSA-**I** and BSA-**2** study, the plot of F_0/F vs [Q] (Figures SI-7a and SI-7b) did not give a linear plot which is the usual case but gave a curve upward towards the y-axis. This is a keen observation of competitive quenching wherein both dynamic and static quenching of the fluorophore are in action. This unusual case was solved by using the Stern-Volmer modified equation given in Eq. (5) [61].

$$\frac{F_0}{F} = (1 + K_D[Q])(1 + K_S[Q]) \quad (5)$$

where K_D and K_S are the dynamic and static quenching constants respectively. The values of K_D and K_S and the respective k_q values for BSA-**I** and BSA-**2** are given in Table 3.

Table 3
Binding and quenching parameters of BSA-**I** and BSA-**2** adducts obtained from fluorescence measurements at 298 K.

Compound	n	K_a	K_S (mol^{-1})	K_D (mol^{-1})	k_q ($mol^{-1}s^{-1}$)
I	1.84	1.62×10^5	4.84×10^5	1.42×10^6	2.45×10^{14}
2	1.70	2.14×10^5	5.82×10^5	1.35×10^6	2.33×10^{14}

The high values of quenching rate and biomolecular quenching constants in addition to the non-linear SV plots direct attention towards the dominancy of static quenching via ground state complex formation. Hence, static quenching majorly contributes for the overall quenching of BSA fluorescence profile [62,63]. A graph of log (F_0–F)/F vs log [Q] was plotted [60,64] to find the total binding sites (n), the slope of which gave the value of n (using eq. 6).

$$log\left(\frac{F_0 - F}{F}\right) = logK_a + nlog[Q] \quad (6)$$

The value of n was calculated to be about 2 in the case of both **I** and **2** which indicates that the molar ratio of protein and compounds in the

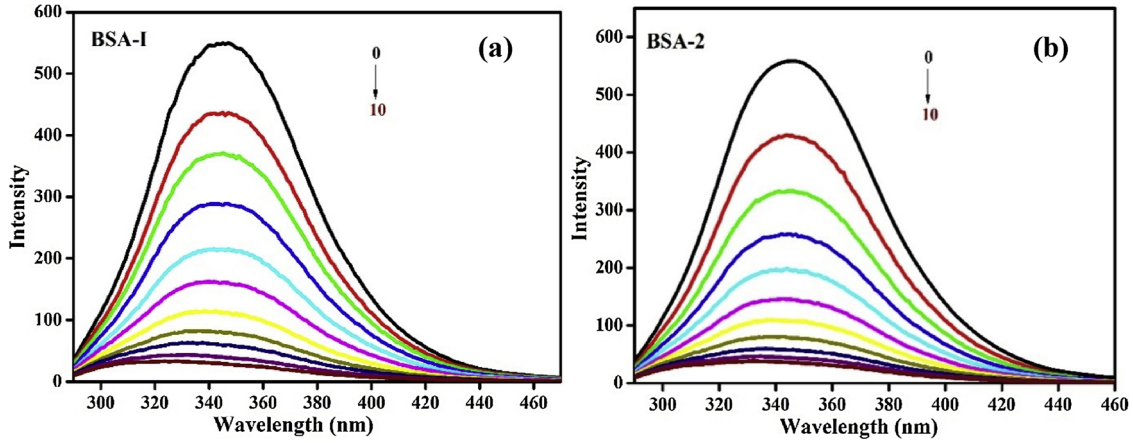

Fig. 8. Intrinsic BSA fluorescence quenching profile with the titration of different concentrations of **(a)** H_2hpdbal-sbdt (**I**) and **(b)** [{V^VO(hpdbal-sbdt)}$_2\mu$-O] **(2)**.

binding response is 1:2. K_a is the binding constant which was calculated using the Benesi-Hildebrand modified equation (Eq. (7)) [61].

$$\frac{F_0}{(F - F_0)} = \left(\frac{b}{a - b}\right)\left(\frac{1}{K_a[Q]} + 1\right) \quad (7)$$

where a and b are both constants. K_a is given by (Table 3) the value of intercept/slope in the plot of $F_0/(F\text{-}F_0)$ vs $1/[Q]$ (Figures SI-8a and SI-8b). Both $[\{V^{V}O(hpdbal\text{-}sbdt)\}_2\mu\text{-}O]$ and H_2hpdbal-sbdt exhibited optimal binding constant values indicating good binding abilities with BSA. This observation can be reasoned by the hydrogen bonding between the phenoxide –O of the ligand and the amino groups of BSA [61,64].

3.4.2. Synchronous fluorescence study

Introduced by Lloyd and Evett in 1970s [65], this technique can gather information about the molecular environment in the vicinity of the fluorophore molecules. Fluorescence of BSA is majorly contributed by two amino acids tyrosine (Tyr) and tryptophan (Trp). To measure their fluorescence simultaneously in a synchronized way, wavelength interval of $\Delta\lambda = 15$ nm (Figures SI-9a and SI-9b) and $\Delta\lambda = 60$ nm (Figures SI-10a and SI-10b) for Tyr and Trp respectively were set and the scan was set between $\lambda_{ex} = 200–350$ nm and $\lambda_{em} = 290–500$ nm to collect information on the quenching brought about by them [61]. The intensity peak for Trp got quenched to a higher extent in comparison to that of the Tyr peak. Therfore, the inference was drawn that the compounds quenched BSA fluorescence mostly by Trp quenching which was evident from the Fig. 9a and b.

3.4.3. 3D fluorescence study

Three dimensional fluorescence spectroscopy aids in examining the representative conformational variations of BSA in a more reliable fashion by deciphering the fluorescence information of in a very comprehensive way [66]. Three optimal concentrations (0.83 μM, 4.17μM, 8.30 μM) of the ligand and $[\{V^{V}O(hpdbal\text{-}sbdt)\}_2\mu\text{-}O]$ were titrated with BSA (5 μM) taken in phosphate buffer of pH 7.4 at 298 K. The spectra were recorded between excitation wavelength of 200–360 nm and emission wavelength of 200–650 nm at a scan rate of 600 nm/min and an increment of 2 nm. Fig. 10 represents the 3D fluorescence spectra and the contour diagrams of BSA-$[\{V^{V}O(hpdbal\text{-}sbdt)\}_2\mu\text{-}O]$ (**2**) adducts and these representations were similar to the 3D spectra of the BSA-ligand adducts (Figure SI-11).

Sharp peaks **a** and **b** in Fig. 10 are due to 1st order Rayleigh scattering ($\lambda_{em} = \lambda_{ex}$) and 2nd order Rayleigh scattering ($\lambda_{em} = 2\lambda_{ex}$) respectively. Peak **1** appears due to the π→π* transitions of the aromatic amino acids, i.e. mainly due to Trp intrinsic fluorophore residues of protein. Peak **2** being the strongest peak is observed as a result of the typical n→π* transition occurring in the polypeptide backbone [67]. Intensities of both these peaks (Table 4) slowly diminished upon subsequent addition of the compounds giving a direct implication that protein peptide strand alterations and amino acid quenching are two important observational effects. Hence, through the 3D fluorescence studies, it is inferred that conformational changes are occurring to BSA due to slow unfolding of protein polypeptide chain with the addition of quencher compounds.

3.4.4. UV–vis study

The absorbance shown by BSA depends mainly on the microenvironment of BSA chromophores and hence the essential parameters to determine the complex formation between BSA and compounds using UV–vis studies are the absorbance bands observed due to amide (-CONH) groups and Trp amino acid residues [67] at 201 nm (strong) and 280 nm (comparatively weaker) respectively. The absorption spectra of BSA (5μM) in phosphate buffer of pH 7.4 upon titration with different concentrations of ligand and $[\{V^{V}O(hpdbal\text{-}sbdt)\}_2\mu\text{-}O]$ (0.83 μM to 8.26 μM each) at 298 K are presented in Figs. 11a and 11b respectively. It was found that with increasing concentrations of compounds, the absorbance shown by pure BSA increased which proposed static quenching [68] for the BSA-**I** and BSA-**2** interaction.

Using the UV absorbance data, double reciprocal plot $(A_0/(A–A_0)$ vs $1/c)$ (Figures SI-12a and SI-12b) was drawn from which association constant K_a for each temperature was found. Van't Hoff's plot ($\ln K_a$ vs $1/T$) using Eq. (8) was drawn to probe the type of forces between BSA and compounds (**I** and **2**) and the thermodynamic parameters involved in the binding reaction (Figures SI-13a and SI-13b).

$$lnK_a = -\frac{\Delta H}{RT} + \frac{\Delta S}{R} \quad (8)$$

The free energy relation given by Eq. (9) was used to calculate Gibbs free energy change ΔG at different temperatures.

$$\Delta G = \Delta H - T\Delta S \quad (9)$$

The values of association constant K_a and free energy change ΔG at four different temperatures are summarized in Table 5. It was observed that the values of all thermodynamic parameters ΔH, ΔS and ΔG are negative which is suggestive of hydrogen bonded or van der Waals interactions between BSA and compounds (**I** and **2**) [69,70] and that the interaction between them is purely spontaneous.

3.4.5. Forster resonance energy transfer (FRET) study

FRET is a phenomenon of transfer of electromagnetic energy non-radiatively to an acceptor quencher present in the ground state from a photo excited donor fluorophore lying in its proximity [71]. In our studies, the fluorophore protein is considered as a donor and the quencher molecule is regarded as an acceptor.

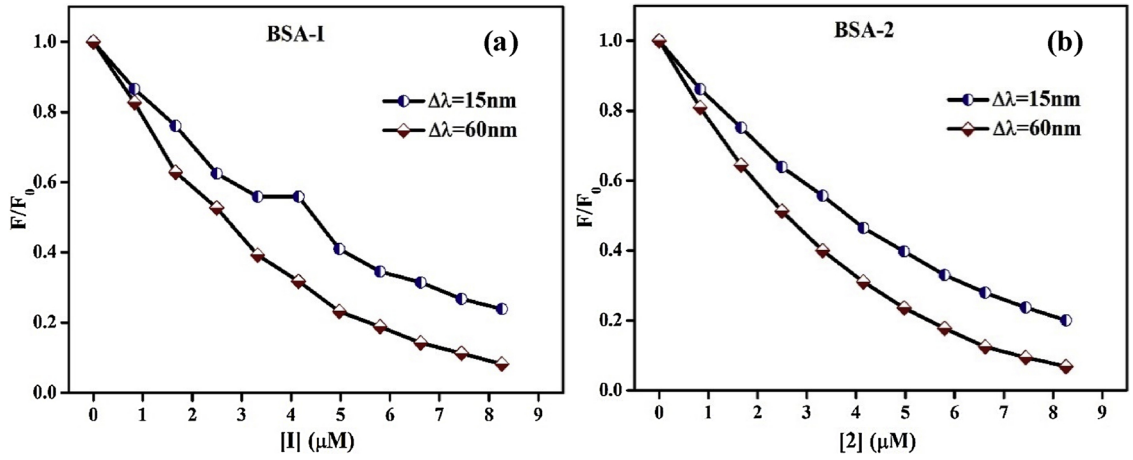

Fig. 9. Graphs obtained from synchronous fluorescence measurements at $\Delta\lambda = 15$ and $\Delta\lambda$ 60 nm for **(a)** BSA-**I** adduct and **(b)** BSA-**2** adduct.

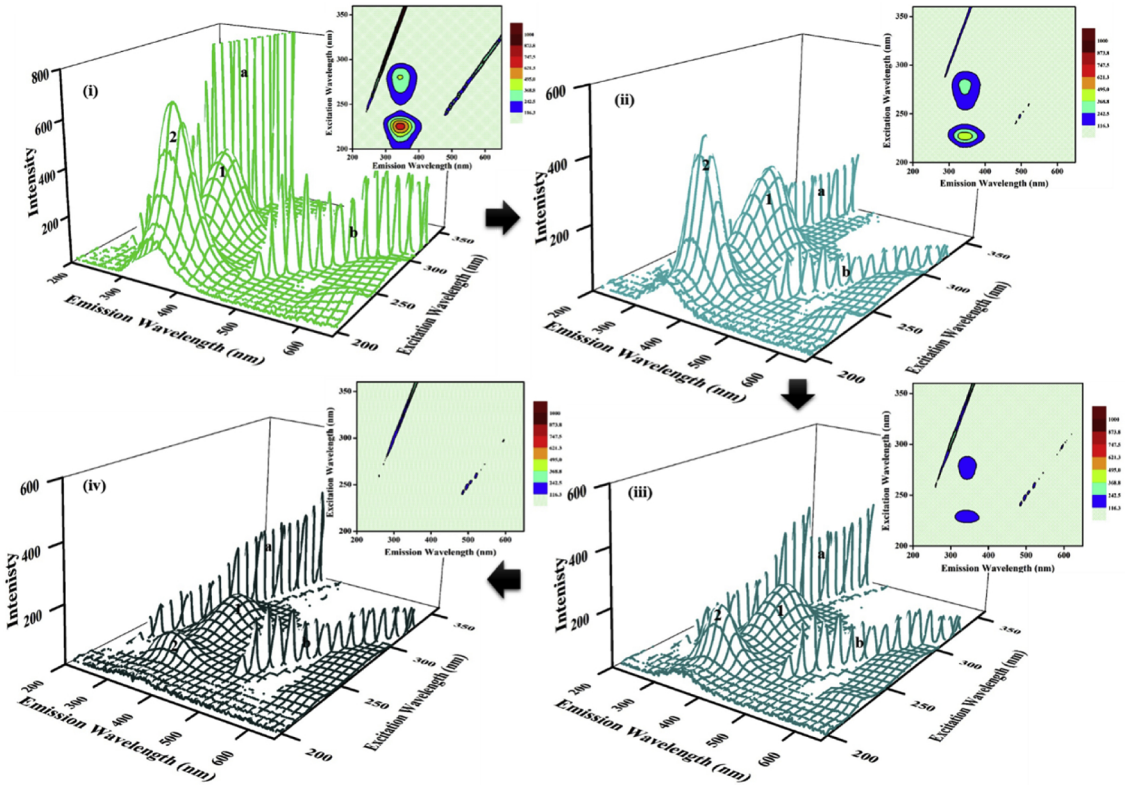

Fig. 10. 3D fluorescence spectra along with the contour diagrams for **(i)** pure BSA (5μM), **(ii)** BSA (5μM)–**2** (0.83 μM), **(iii)** BSA (5μM)–**2** (4.17μM) and **(iv)** BSA (5μM)–**2** (8.30 μM).

Table 4
Fluorescence peak (peak **1** and peak **2**) changes observed from 3D fluorescence studies.

Samples	Peak 1					Peak 2				
	λ_{ex} (nm)	λ_{em} (nm)	Intensity	Stokes shift Δλ(nm)	% quench	λ_{ex} (nm)	λ_{em} (nm)	Intensity	Stokes shift Δλ (nm)	% quench
BSA	280	348	379.73	68	–	224	344	676.67	120	–
I_a	280	348	355.97	68	6.26	228	342	476.12	114	29.64
I_b	280	346	179.54	66	52.72	230	338	189.37	108	72.01
I_c	280	336	81.42	56	78.56	230	334	70.76	104	89.54
2_a	280	338	282.36	58	25.64	226	342	457.24	116	32.43
2_b	280	342	156.45	62	58.80	228	344	196.22	116	71.00
2_c	280	336	95.38	56	74.88	230	336	81.50	106	87.96

$\mathbf{I_a}$: BSA (5 μM) + **I** (0.83 μM), $\mathbf{I_b}$: BSA (5 μM) + **I** (4.17 μM), $\mathbf{I_c}$:BSA (5 μM) + **I** (8.30 μM).
$\mathbf{2_a}$: BSA (5 μM) + **2** (0.83 μM), $\mathbf{2_b}$: BSA (5 μM) + **2** (4.17 μM), $\mathbf{2_c}$:BSA (5 μM) + **2** (8.30 μM).

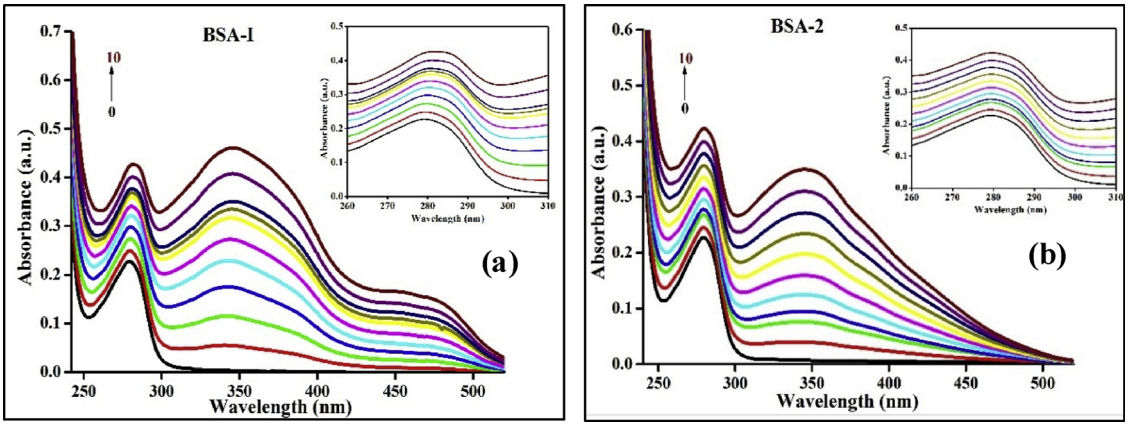

Fig. 11. UV–vis absorption spectra of BSA upon titration with different concentrations of **(a)** H_2hpdbal-sbdt (**I**) and **(b)** [{V^{V}O(hpdbal-sbdt)}$_2$μ-O] **(2)**.

Table 5
Binding and thermodynamic parameters acquired from UV–vis titration studies.

Sample	T (K)	K_a	ΔH (kJ)	ΔS (J/K/mol)	ΔG (kJ/mol)
BSA-I	293	2.99×10^4	−40.48	-52.39	−25.13
	298	2.29×10^4			−24.87
	303	1.79×10^4			−24.61
	308	1.32×10^4			−24.34
BSA-2	293	3.32×10^4	−71.86	−158.06	−25.55
	298	2.47×10^4			−24.76
	303	1.34×10^4			−23.18
	308	0.82×10^4			−23.97

Fig. 12a and b depicts the overlap integral of the fluorescence emission spectrum of BSA and the absorption spectrum of **I** and **2** respectively. The energy transferred was calculated using the FRET theory [67] (using Eq. (10)).

$$E = 1 - \frac{F_0}{F} = \frac{R_0^6}{R_0^6 + r^6} \quad (10)$$

where E is the energy transfer efficiency, F_0 is the fluorescence intensity of pure BSA, F is the fluorescence intensity of BSA added with the quencher compound and r is the binding site proximity between fluorophore and quencher molecules. The Forster critical energy transfer distance (R_0) at which there is an energy transfer efficiency of 50% was calculated using Eq. (11).

$$R_0^6 = 8.79 \times 10^{-25} K^2 N^{-4} \Phi J \quad (11)$$

where $K^2 = 2/3$ is the spatial orientation factor for BSA, N = 1.336 is the average refractive index of the medium, ϕ = 0.15 is the fluorescence quantum yield [72] and *J* is the overlap integral of the absorption spectrum of compounds (**I** and **2**) and fluorescence emission spectrum of BSA. This value was obtained using Eq. (12).

$$J = \frac{\int_0^\infty F(\lambda)\varepsilon(\lambda)\lambda^4 d\lambda}{\int_0^\infty F(\lambda) d\lambda} \quad (12)$$

where F(λ) is the corrected fluorescence intensity of the fluorophore BSA over a wavelength range of λ to (λ + dλ). ε(λ) is the molar extinction coefficient of the acceptor compounds at λ [73]. Using all the above equations, *J*, E, R_0 and r were calculated and the values obtained are given in Table 6. According to the rules laid by the Förster non-radiation energy transfer theory [73], the proximity of binding sites **r** should be in between 2 to 8 nm with a condition that 0.5 R_0 < r < 1.5 R_0. The present case of BSA-**I** and BSA-**2** interactions are in agreement with the above rules hence demonstrating high energy transfer probability from excited state BSA molecules to the ground state quencher

Table 6
Energy transfer parameters calculated for the binding of compounds with BSA.

Sample	J (cm^3/L/mol)	E	R_0 (nm)	r (nm)
BSA-I	2.81×10^{-14}	0.79	2.99	2.41
BSA-2	3.42×10^{-14}	0.80	3.10	2.47

compounds. FRET study supplements our observation of BSA fluorescence quenching through static mechanism [74] by the compounds **I** and **2**.

3.4.6. IR binding study

The protein and polypeptide IR spectra exhibit distinctive fingerprint Amide I bands due to the C═O stretching and Amide II bands due to the N−H bending associated with the amide bonds linking the amino acid chains. Both bands are sensitive [75] to the secondary structure of the protein. This feature can be used as a probe to investigate the conformational changes in the secondary structure of BSA as both C═O and the N−H groups are involved in intramolecular hydrogen bonding between different elements of the secondary structure [76]. To investigate the influence of compound **2** on the secondary structure conformations of BSA, IR spectral studies were carried by titrating three optimal concentrations of **2** (17 μM, 83 μM and 165 μM) with BSA (100 μM). Amide I and amide II bands were observed at 1649 cm^{-1} and 1539 cm^{-1} respectively in the original BSA spectrum. A shoulder peak around 1468 cm^{-1} was also seen. These observations confirm the α-helical conformational dominancy of the native BSA structure. Incubation of the compounds with BSA produced small shifts in the IR spectra (Table SI-3). The amide I band is usually used as a better predictor for quantifying the secondary structure of proteins when compared to amide II band even though precisely resolved peaks does not appear in both the cases. The problem of analyzing the amount of different forms of BSA secondary structure was tackled by performing peak fitting on the Amide I band in the wavenumber region of 1600-1700 cm^{-1} in the IR second derivative spectra. This peak fitting was done with the help of Levenberg- Marquardt (L–M) algorithm [77] which provided neatly resolved spectra for different secondary structure confirmations of the protein as shown in Fig. 13. The same method was used to analyse the conformational changes occurring in the protein on addition of ligand **I** (Figure SI-14).

The information on the secondary structure forms of BSA obtained by resolving the IR spectra of samples is represented in Table 7. The conversion of α-helical form into β-helical and other minor forms with the concentration of compounds deliberates that the coiled BSA secondary structure unfolds in a progressive and steady manner.

All these spectroscopic investigations concludes that the carrier proteins can transport the novel drug candidate [{V^VO(hpdbal-sbdt)}$_2$μ-O] (**2**) to the targeted site of action in a hassle-free manner

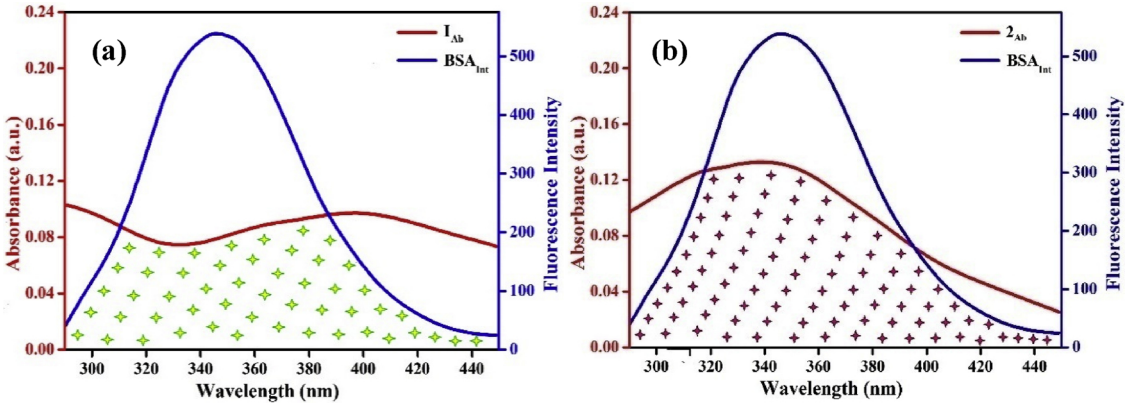

Fig. 12. Depiction of BSA fluorescence intensity overlap with the absorbance of (**a**) H_2hpdbal-sbdt (**I**) and (**b**) [{V^VO(hpdbal-sbdt)}$_2$μ-O] (**2**).

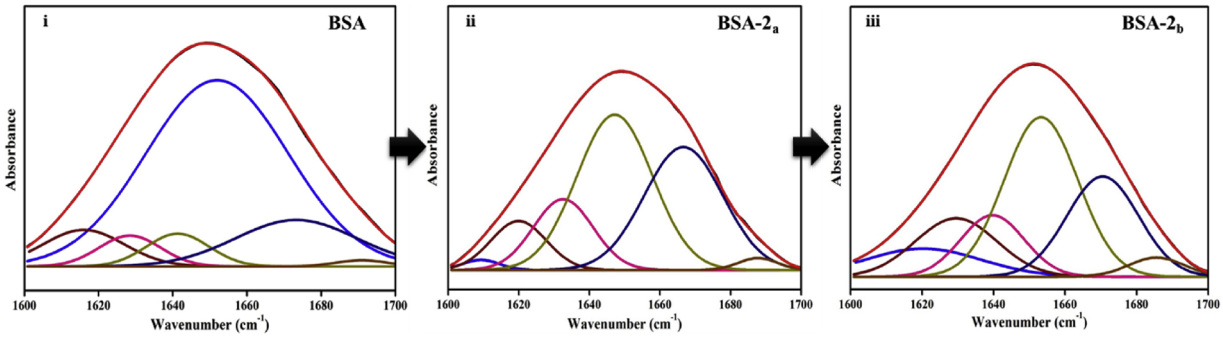

Fig. 13. Peak fitted deconvoluted IR Spectrum of **(i)** pure BSA (100 μM), BSA-**2** (17 μM) and **(iii)** BSA-**2** (83 μM).

Table 7
The percentages of different BSA secondary structure conformations obtained from the deconvoluted Amide I IR band.

Sample		α-helix		β-sheet		Random coil		Turn		β-antiparallel	
		cm^{-1}	%	cm^{-1}	%	cm^{-1}	%	cm^{-1}	%	cm^{-1}	%
BSA		1652	68	1616,1628	12	1641	5	1673	14	1691	1
I	I_a	1650	41.6	1615,1626	15.6	1636	12.7	1671	27.6	1690	2.5
	I_b	1654	38.7	1622,1629	18.1	1640	14.3	1670	26.2	1686	2.6
2	2_a	1647	40.3	1609,1620	10.4	1633	14.5	1667	33.2	1688	1.6
	2_b	1653	37.4	1620,1630	24.1	1640	12.4	1671	22.8	1686	3.3

I_a: BSA (100 μM) + **I** (17 μM), **I_b**: BSA (100 μM) + **I** (83 μM).
2_a: BSA (100 μM) + **2** (17 μM), **2_b**: BSA (100 μM) + **2** (83 μM).

without momentously affecting the structure and function of the proteins. These studies can also be used as supporting information in the future drug development processes with respect to *in vivo* studies or clinical trials.

4. Conclusions

Novel oxidovanadium [$V^{V}O(OCH_3)$(hpdbal-sbdt)] (**1**) and μ-oxo bridged oxidovanadium [{$V^{V}O$(hpdbal-sbdt)}$_2$μ-O] (**2**) complexes were obtained by the reaction of [$V^{IV}O(acac)_2$] and the ligand H_2hpdbal-sbdt (**I**). Dinuclear vanadium complex [{$V^{V}O$(hpdbal-sbdt)}$_2$μ-O] **(2)** was revealed to be a potential anticancer molecule due to its ability to inhibit proliferation of breast and lung cancer cells, induce apoptosis and reproductive cell death. The activity was found to be comparable with the standard cisplatin drug. The compound **2** was also found to be stable enough at physiological pH condition and was studied for the interaction with protein alongside the ligand for comparison studies. The interaction study of BSA-vanadium complex (**2**) gave a conclusive remark that the binding is spontaneous and exothermic. A hydrogen bonded or van der Waals type of interaction between the protein and the anticancer complex was revealed. The study also indicated high probability of energy transfer to quencher compounds from BSA via static quenching mechanism. In addition, the α-helical content of the protein decreased only when titrated with higher concentrations of the compound. These arguments will hence support our assertion that the oxidovanadium complex **2** can pass the blood stream without affecting the normal functioning of the serum protein in healthy cells.

Declarations of interest

None

Acknowledgements

This work was supported by Science and Engineering Research Board (SERB), Department of Science and Technology (DST), India [SB/FT/CS-100/2013]; Centre for Nano and Material Sciences, Jain University, Bangalore, India; Nanomission, DST, India [SR/NM/NS-20/2014].

Appendix A. Supplementary data

Supplementary material related to this article can be found, in the online version, at doi:https://doi.org/10.1016/j.jtemb.2018.10.019.

References

[1] J. Ferlay, I. Soerjomataram, M. Ervik, R. Dikshit, S. Eser, GLOBOCAN 2012: Cancer Incidence and Mortality Worldwide, Lyon, France (2013).
[2] B.W. Stewart, C.P. Wild, World Cancer Report, Lyon, France (2014).
[3] (a) T.W. Hambley, Developing new metal-based therapeutics: challenges and opportunities, Dalton Trans. (2007) 4929–4937;
(b) S. Kuntikana, C. Bhat, M. Kongot, S.I. Bhat, A. Kumar, An expeditious green cascade synthesis of 3-arylideneaminoquinazolin- 4(1H)-one derivatives via 'solvent drop grinding' and their antioxidant and DNA protective studies, Chem. Sel. 1 (2016) 1723–1728;
(c) C. Bhat, A. Kumar, Synthesis of allokainic acid: a review, Asian J. Org. Chem. 4 (2015) 102–115;
(d) M. Kongot, A. Kumar, Metals in medicines, Sci. Rep. 55 (2018) 41–43.
[4] C. Orvig, M.J. Abrams, Medicinal inorganic chemistry: introduction, Chem. Rev. 99 (1999) 2201–2204.
[5] C. Santini, M. Pellei, V. Gandin, M. Porchia, F. Tisato, C. Marzano, Advances in copper complexes as anticancer agents, Chem. Rev. 114 (2014) 815–862.
[6] K.H. Thompson, C. Orvig, Metal complexes in medicinal chemistry:New vistas and challenges in drug design, Dalton Trans. (2006) 761–764.
[7] B. Rosenberg, Platinum Complexes for the Treatment of Cancer. Why the Search goes on, Wiley, New York, 1999.
[8] F. Arnesano, G. Natile, Mechanistic insight into the cellular uptake and processing of cisplatin 30 years after its approval by FDA, Coord. Chem. Rev. 253 (2009) 2070–2081.
[9] I. Ott, R. Gust, Non platinum metal complexes as anti-cancer drugs, Archiv der Pharmazie 340 (2007) 117–126.
[10] Y. Jung, S.J. Lippard, Direct cellular responses to platinum-induced DNA damage, Chem. Rev. 107 (2007) 1387–1407.
[11] D. Lebwohl, R. Canetta, Clinical development of platinum complexes in cancer therapy: an historical perspective and an update, Eur. J. Cancer 34 (1998) 1522–1534.
[12] G. Markus, A.J. Michael, K.K. Bernhard, Update of the preclinical situation of anticancer platinum complexes: novel design strategies and innovative analytical approaches, Curr. Med. Chem. 12 (2005) 2075–2094.
[13] P.C.A. Bruijnincx, P.J. Sadler, New trends for metal complexes with anticancer activity, Curr. Opin. Chem. Biol. 12 (2008) 197–206.
[14] D. Rehder, Biological and medicinal aspects of vanadium, Inorg. Chem. Commun. 6

(2003) 604–617.
[15] H. Michibata, Vanadium-Biochemical and Molecular Biological Approaches, Springer, New York, 2012, https://doi.org/10.1007/978-94-007-0913-3.
[16] R. Sankar Ray, B. Ghosh, A. Rana, M. Chatterjee, Suppression of cell proliferation, induction of apoptosis and cell cycle arrest: chemopreventive activity of vanadium in vivo and in vitro, Int. J. Cancer 120 (2006) 13–23.
[17] (a) M.R. Maurya, A.A. Khan, A. Azam, S. Ranjan, N. Mondal, A. Kumar, F. Avecilla, J.C. Pessoa, Vanadium complexes having [VIVO]2+ and [VVO2]+ cores with binucleating dibasic tetradentate ligand: synthesis, characterization, catalytic and antiamoebic activities, Dalton Trans. 39 (2010) 1345–1360;
(b) M.R. Maurya, M. Bisht, N. Chaudhary, A. Kumar, F. Avecilla, J.C. Pessoa, Spectroscopic and structural characterization of noninnocent mixed-ligand oxidovanadium(V) complexes, Eur. J. Inorg. Chem. (2012) 4846–4855.
[18] M.R. Maurya, A. Kumar, M. Abid, A. Azam, Dioxovanadium (V) and μ-oxo bis [oxovanadium (V)] complexes containing thiosemicarbazone based ONS donor set and their antiamoebic activity, Inorg. Chim. Acta 359 (2006) 2439–2447.
[19] M.R. Maurya, A. Kumar, A.R. Bhat, A. Azam, C. Bader, D. Rehder, Synthesis, characterization, reactivity, and catalytic potential of model vanadium (IV, V) complexes with benzimidazole-derived ONN donor ligands, Inorg. Chem. 45 (2006) 1260–1269.
[20] J.C. Pessoa, S. Etcheverry, D. Gambino, Vanadium compounds in medicine, Coord. Chem. Rev. 301–302 (2015) 24–48.
[21] (a) M.R. Maurya, A.A. Khan, A. Azam, A. Kumar, S. Ranjan, N. Mondal, J.C. Pessoa, Dinuclear oxidovanadium(IV) and dioxidovanadium(V) complexes of 5,5′- methylenebis(dibasic tridentate) ligands: synthesis, spectral characterisation, reactivity, and catalytic and antiamoebic activities, Eur. J. Inorg. Chem. 35 (2009) 5377–5390;
(b) A. Shankar, M. Kongot, V.K. Saini, A. Kumar, Removal of pentachlorophenol pesticide from aqueous solutions using modified chitosan, Arab. J. Chem. (2018), https://doi.org/10.1016/j.arabjc.2018.01.016 in press.
[22] T. Mukherjee, J. Costa Pessoa, A. Kumar, A.R. Sarkar, Oxidovanadium(IV) Schiff Base complex derived from vitamin B6: synthesis, characterization, and insulin enhancing properties, Inorg. Chem. 50 (2011) 4349–4361.
[23] H. Radim, S. Pavel, C. Jana, S. Alena, V. Jirina, V. Jaromir, K. Jiri, R. Martina, Differences in vanadocene dichloride and cisplatin effect on MOLT-4 leukemia and human peripheral blood mononuclear cells, Med. Chem. 8 (2012) 615–621.
[24] (a) M.R. Maurya, A. Arya, U. Kumar, A. Kumar, F. Avecilla, J.C. Pessoa, Polymer-bound oxidovanadium(IV) and dioxidovanadium(V) complexes: synthesis, characterization and catalytic application for the hydroamination of styrene and vinyl pyridine, Dalton Trans. (2009) 9555–9566;
(b) A. Evangelou, S. Karkabounas, G. Kalpouzos, M. Malamas, R. Liasko, D. Stefanou, A.T. Vlahos, T.A. Kabanos, Comparison of the therapeutic effects of two vanadium complexes administered at low doses on benzo[a]pyrene- induced malignant tumors in rats, Cancer Lett. 119 (1997) 221–225.
[25] K.H. Thompson, C. Orvig, Coordination chemistry of vanadium in metallo-pharmaceutical candidate compounds, Coord. Chem. Rev. 219–221 (2001) 1033–1053.
[26] O.Y. Abakumova, O.V. Podobed, N.F. Belayeva, A.I. Tochilkin, Anticancer activity of oxovanadium compounds, Biochem. (Mosc.) Suppl. Ser. B: Biomed. Chem. 6 (2012) 164–170.
[27] C. Djordjevic, S.A. Craig, E. Sinn, A polymeric peroxo heteroligand vanadate(V). Synthesis, spectra, and structure of MI[VO(O2)(C4H5O4N)], Inorg. Chem. 24 (1985) 1281–1283.
[28] E. Kioseoglou, S. Petanidis, C. Gabriel, A. Salifoglou, The chemistry and biology of vanadium compounds in cancer therapeutics, Coord. Chem. Rev. 301–302 (2015) 87–105.
[29] S. Banerjee, A. Dixit, R.N. Shridharan, A.A. Karande, A.R. Chakravarty, Endoplasmic reticulum targeted chemotherapeutics: the remarkable photo-cytotoxicity of an oxovanadium(IV) vitamin-B6 complex in visible light, Chem. Commun. 50 (2014) 5590–5592.
[30] (a) K.H. Thompson, K. Böhmerle, E. Polishchuk, C. Martins, P. Toleikis, J. Tse, V. Yuen, J.H. McNeill, C. Orvig, Complementary inhibition of synoviocyte, smooth muscle cell or mouse lymphoma cell proliferation by a vanadyl curcumin complex compared to curcumin alone, J. Inorg. Biochem. 98 (2004) 2063–2070;
(b) S. Banerjee, I. Pant, I. Khan, P. Prasad, A. Hussain, P. Kondaiah, A.R. Chakravarty, Remarkable enhancement in photocytotoxicity and hydrolytic stability of curcumin on binding to an oxovanadium (IV) moiety, Dalton Trans. 44 (2015) 4108–4122.
[31] (a) S.A. Chowdhury, K. Kishino, R. Satoh, K. Hashimoto, H. Kikuchi, Tumor-specificity and apoptosis-inducing activity of stilbenes and flavonoids, Anticancer. Res. 25 (2005) 2055–2064;
(b) O.J. D'Cruz, Y. Dong, F.M. Uckun, Spermicidal activity of oxovanadium(IV) complexes of 1,10-phenanthroline, 2,2'-bipyridyl, 5'-bromo-2'- hydroxyacetophenone and derivatives in humans, Biol. Reprod. 60 (1999) 435–444.
[32] S. Lorin, A. Hamaï, M. Mehrpour, P. Codogno, Autophagy regulation and its role in cancer, Semin. Cancer Biol. 23 (2013) 361–379.
[33] Z. Khan, P.S. Bisen, Oncoapoptotic signaling and deregulated target genes in cancers: Special reference to oral cancer, Biochim. Biophys. Acta 1836 (2013) 123–145.
[34] S. Petanidis, E. Kioseoglou, M. Hadzopoulou-Cladaras, A. Salifoglou, Novel ternary vanadium-betaine-peroxido species suppresses H-ras and matrix metalloproteinase-2 expression by increasing reactive oxygen species-mediated apoptosis in cancer cells, Cancer Lett. 335 (2013) 387–396.
[35] P. Anitha, R. Manikandan, P. Vijayan, G. Prakash, P. Viswanathamurthi, R.J. Butcher, Nickel(II) complexes containing ONS donor ligands: synthesis, characterization, crystal structure and catalytic application towards C-C cross-coupling reactions, J. Chem. Sci. 127 (2015) 597–608.
[36] (a) F. Korkmaz, D.A. Erdogan, S. Ozalp-Yaman, Interaction of a novel platinum drug with bovine serum albumin: FTIR and UV-Vis spectroscopy analysis, New J. Chem. 39 (2015) 5676–5685;
(b) N. Maurya, M. Parray, J.K. Maurya, A. Kumar, R. Patel, Interaction of promethazine and adiphenine to human hemoglobin:A comparative spectroscopic and computational analysis, Spectrochim. Acta A: Mol. Biomol. Spectrosc. 199 (2018) 32–42;
(c) B. Aneja, M. Kumari, A. Azam, A. Kumar, M. Abid, R. Patel, Effect of triazole-tryptophan hybrid on the conformation stability of bovine serum albumin, Luminescence 33 (2018) 464–474.
[37] (a) D. Senthil Raja, N.S.P. Bhuvanesh, K. Natarajan, Effect of N(4)-phenyl substitution in 2-oxo-1,2-dihydroquinoline-3-carbaldehyde semicarbazones on the structure, DNA/protein interaction, and antioxidative and cytotoxic activity of Cu (II) complexes, Inorg. Chem. 50 (2011) 12852–12866;
(b) J.K. Maurya, A.B. Khan, N. Dohare, A. Ali, A. Kumar, R. Patel, Effect of aromatic amino acids on the surface properties of 1-dodecyl-3- (4-(3-dodecylimidazolidin-1-yl)butyl)imidazolidine bromide gemini surfactant, J. Disp. Sci. Tech. 39 (2018) 174–180.
[38] (a) X.M. He, D.C. Carter, Atomic structure and chemistry of human serum albumin, Nature 358 (1992) 209–215;
(b) M. Kongot, N. Maurya, N. Dohare, Mud. Parray, J.K. Maurya, A. Kumar, R. Patel, Enthalpy-driven interaction between dihydropyrimidine compound and bovine serum albumin: a spectroscopic and computational approach, J. Biomol. Struct. Dyn. 36 (2018) 1161–1170;
(c) T. Mukherjee, J. Costa Pessoa, A. Kumar, A.R. Sarkar, Synthesis, structure, magnetic properties and biological activity of supramolecular copper(II) and nickel (II) complexes with a Schiff base ligand derived from vitamin B6, Dalton Trans. 42 (2013) 2594–2607;
(d) T. Mukherjee, J.C. Pessoa, A. Kumar, A.R. Sarkar, Formation of an unusual pyridoxal derivative: characterization of Cu(II), Ni(II) and Zn(II) complexes and evaluation of binding to DNA and to human serum albumin, Inorg. Chim. Acta 426 (2015) 150–159;
(e) P.J. Sadler, A. Tucker, J.H. Viles, Involvement of a lysine residue in the N-terminal Ni2+ and Cu2+ binding site of serum albumins, Eur. J. Biochem. 220 (1994) 193–200.
[39] R.A. Rowe, M.M. Jones, Vanadium(IV)oxy(Acetylacetonate), Inorganic Syntheses, Wiley, New York, USA, 1957.
[40] (a) R. Botros, Azomethine Dyes Derived from an o-Hydroxy Aromatic Aldehyde and 2-Aminopyridine, United States Patent, 1977;
(b) M. Akbar Ali, M.T.H. Tarafdar, Metal complexes of sulphur and nitrogen-containing ligands: complexes of s- benzyldithiocarbazate and a Schiff base formed by its condensation with pyridine-2- carboxaldehyde, J. Inorg. Nucl. Chem. (1977), pp. 1785–1791.
[41] M. Kongot, N. Dohare, V. Singh, N.K. Singhal, R. Patel, A. Kumar, A novel biocompatible NiII tethered moiety as a glucose uptake agent and a hit against methicillin- resistant Staphylococcus aureus, Eur. J. Pharm. Sci. 123 (2018) 335–349.
[42] A.W. Addison, T.N. Rao, J. Reedijk, J. van Rijn, G.C. Verschoor, Synthesis, structure, and spectroscopic properties of copper(II) compounds containing nitrogen-sulphur donor ligands; The crystal and molecular structure of aqua[1,7-bis(N-methylbenzimidazol-2'-yl)- 2,6-dithiaheptane]copper(II) perchlorate, J. Chem. Soc. Dalton Trans. (1984) 1349–1356.
[43] M.R. Maurya, C. Haldar, A.A. Khan, A. Azam, A. Salahuddin, A. Kumar, J.C. Pessoa, Synthesis, characterization, catalytic and antiamoebic activity of vanadium complexes of binucleating bis(dibasic tridentate ons donor) ligand systems, Eur. J. Inorg. Chem. 2012 (2012) 2560–2577.
[44] F. Ahmed, R. Dewani, M.K. Pervez, S.J. Mahboob, S.A. Soomro, Non-destructive FT-IR analysis of mono azo dyes, Bulg. Chem. Commun. 48 (2016) 71–77.
[45] D. Marion, An introduction to biological NMR spectroscopy, Mol. Cell. Proteom. 12 (2013) 3006–3025.
[46] D. Rehder, C. Weidemann, A. Duch, W. Priebsch, Vanadium-51 shielding in vanadium(V) complexes: a reference scale for vanadium binding sites in biomolecules, Inorg. Chem. 27 (1988) 584–587.
[47] M.R. Maurya, B. Sarkar, F. Avecilla, I. Correia, Vanadium(IV and V) complexes of pyrazolone based ligands: synthesis, structural characterization and catalytic applications, Dalton Trans. 45 (2016) 17343–17364.
[48] M.R. Maurya, A. Kumar, M. Ebel, D. Rehder, Synthesis, characterization, reactivity, and catalytic potential of model vanadium(IV, V) complexes with benzimidazole-derived ONN donor ligands, Inorg. Chem. 45 (2006) 5924–5937.
[49] P. Prabhakaran, F. Hassiotou, P. Blancafort, L. Filgueira, Cisplatin induces differentiation of breast cancer cells, Front. Oncol. 3 (2013) 134.
[50] C.-H. Dai, P. Chen, J. Li, T. Lan, Y.-C. Chen, H. Qian, K. Chen, M.-Y. Li, Co-inhibition of pol θ and HR genes efficiently synergize with cisplatin to suppress cisplatin-resistant lung cancer cells survival, Oncotarget 40 (2016) 65157–65170.
[51] I. Correia, S. Roy, C.P. Matos, S. Borovic, N. Butenko, I. Cavaco, F. Marques, J. Lorenzo, A. Rodríguez, V. Morenoe, J.C. Pessoa, Vanadium(IV) and copper(II) complexes of salicylaldimines and aromatic heterocycles: cytotoxicity, DNA binding and DNA cleavage properties, J. Inorg. Biochem. 147 (2015) 134–146.
[52] (a) Y.L. Zhang, X.S. Wang, W. Fang, X.Y. Cai, H.Z. Li, J.W. Mao, X.B. Jin, Y.L. Bai, J.Z. Lu, In vitro study of the cytotoxicities of two mixed-ligand oxovanadium complexes on human hepatoma cells, Die Pharmazie 68 (2013) 827–834;
(b) L. Eloy, A.S. Jarrousse, M.L. Teyssot, Anticancer activity of silver-N-heterocyclic carbene complexes: caspase- independent induction of apoptosis via mitochondrial apoptosis-inducing factor (AIF), ChemMedChem 5 (2012) 805–814.
[53] (a) A.P. Gonçalves, A. Videira, P. Soares, V. Máximo, Orthovanadate-induced cell death in RET/PTC1-harboring cancer cells involves the activation of caspases and altered signaling through PI3K/Akt/mTOR, Life Sci. 89 (2011) 371–377;
(b) M.L. Taddei, E. Giannoni, T.FiaschiP. Chiarugi, Anoikis: an emerging hallmark

in health and diseases, J. Pathol. 226 (2012) 380–393.
[54] G. Völgyi, R. Ruiz, K. Box, J. Comer, E. Bosch, K. Takács-Novák, Potentiometric and spectrophotometric pKa determination of water-insoluble compounds: validation study in a new cosolvent system, Anal. Chim. Acta 583 (2007) 418–428.
[55] (a) D.T. Manallack, R.J. Prankerd, E. Yuriev, T.I. Oprea, D.K. Chalmers, The significance of acid/base properties in drug discovery, Chem. Soc. Rev. 42 (2013) 485–496;
(b) D.S. Reddy, M. Kongot, S.P. Netalkar, M.M. Kurjogi, R. Kumar, F. Avecilla, A. Kumar, Synthesis and evaluation of novel coumarin-oxime ethers as potential anti- tubercular agents: their DNA cleavage ability and BSA interaction study, Eur. J. Med. Chem. 150 (2018) 864–875.
[56] M.R. Maurya, S. Agarwal, C. Bader, M. Ebel, D. Rehder, Synthesis, characterisation and catalytic potential of hydrazonato-vanadium(V) model complexes with [VO] 3+ and [VO2] + cores, Dalton Trans. (2005) 537–544.
[57] W. Plass, A. Pohlmann, H.-P. Yozgatli, N-Salicylidenehydrazides as versatile tridentate ligands for dioxovanadium(V) complexes, J. Inorg. Biochem. 80 (2000) 181–183.
[58] H.N. Po, N.M. Senozan, The henderson-hasselbalch equation: its history and limitations, J. Chem. Educ. 78 (2001) 1499.
[59] K. Das, K. Rawat, R. Patel, H.B. Bohidar, Size-dependent CdSe quantum dot-lysozyme interaction and effect on enzymatic activity, RSC Adv. 6 (2016) 46744–46754.
[60] N. Dohare, A.B. Khan, F. Athar, S.C. Thakur, R. Patel, Urea-induced binding between diclofenac sodium and bovine serum albumin:A spectroscopic insight, Luminescence 31 (2016) 945–951.
[61] V. Gomathi Sankareswari, D. Vinod, A. Mahalakshmi, M. Alamelu, G. Kumaresan, R. Ramaraj, S. Rajagopal, Interaction of oxovanadium(IV)-salphen complexes with bovine serum albumin and their cytotoxicity against cancer, Dalton Trans. 43 (2014) 3260–3272.
[62] P. Banerjee, S. Pramanik, A. Sarkar, S.C. Bhattacharya, Deciphering the fluorescence resonance energy transfer signature of 3-pyrazolyl 2-pyrazoline in transport proteinous environment, J. Phys. Chem. B 113 (2009) 11429–11436.
[63] X. Pan, R. Liu, P. Qin, L. Wang, X. Zhao, Spectroscopic studies on the interaction of acid yellow with bovine serum albumin, J. Lumin. 130 (2010) 611–617.
[64] E. Carter, I.A. Fallis, D.M. Murphy, D.J. Willock, S. Van Doorslaer, E. Vinck, Probing the role of weak outer sphere interactions (H-bonds) in VO(3,5-tBu2-salophen) – epoxide adducts by EPR, ENDOR and HYSCORE, Chem. Phys. Lett. 486 (2010) 74–79.
[65] F. Samari, B. Hemmateenejad, M. Shamsipur, M. Rashidi, H. Samouei, Affinity of two novel five-coordinated anticancer Pt(II) complexes to human and bovine serum albumins: A spectroscopic approach, Inorg. Chem. 51 (2012) 3454–3464.
[66] P. Kalaivani, R. Prabhakaran, E. Vaishnavi, T. Rueffer, H. Lang, P. Poornima, R. Renganathan, V. Vijaya Padma, K. Natarajan, Synthesis, structure, DNA/protein binding and in vitro cytotoxicity of new ruthenium metallates, Inorg. Chem. Front. 1 (2014) 311–324.
[67] (a) C. Jash, P.V. Payghan, N. Ghoshal, G. Suresh Kumar, Binding of the iminium and alkanolamine forms of sanguinarine to lysozyme: spectroscopic analysis, thermodynamics, and molecular modeling studies, J. Phys. Chem. B 118 (2014) 13077–13091;
(b) C. Jash, G.S. Kumar, Binding of alkaloids berberine, palmatine and coralyne to lysozyme:A combined structural and thermodynamic study, RSC Adv. 4 (2014) 12514–12525.
[68] J. Tian, J. Liu, Z. Hu, X. Chen, Probing the binding of scutellarin to human serum albumin by circular dichroism, fluorescence spectroscopy, FTIR, and molecular modeling method, Biorg. Med. Chem. 13 (2005) 4124–4129.
[69] Q. Yang, X.-m. Zhou, X.-g. Chen, Combined molecular docking and multi-spectroscopic investigation on the interaction between Eosin B and human serum albumin, J. Lumin. 131 (2011) 581–586.
[70] (a) B. Ojha, G. Das, The interaction of 5-(alkoxy)naphthalen-1-amine with bovine serum albumin and its effect on the conformation of protein, J. Phys. Chem. B 114 (2010) 3979–3986;
(b) P.D. Ross, S. Subramanian, Thermodynamics of protein association reactions: forces contributing to stability, Biochemistry 20 (1981) 3096–3102.
[71] D. Beljonne, C. Curutchet, G.D. Scholes, R.J. Silbey, Beyond förster resonance energy transfer in biological and nanoscale systems, J. Phys. Chem. B 113 (2009) 6583–6599.
[72] X.-X. Cheng, Y. Lui, B. Zhou, X.-H. Xiao, Y. Liu, Probing the binding sites and the effect of berbamine on the structure of bovine serum albumin, Spectrochim. Acta A: Mol. Biomol. Spectrosc. 72 (2009) 922–928.
[73] M. Asadi, Z. Asadi, S.B. Sadi, L. Zarei, F.M. Baigi, Z. Amirghofran, Synthesis, characterization and the interaction of some new water-soluble metal Schiff base complexes with human serum albumin, Spectrochim. Acta A:Mol. Biomol. Spectrosc. 122 (2014) 118–129.
[74] J.R. Lakowicz, in Principles of Fluorescence Spectroscopy. Ed. 2, Springer, Boston, MA, 2006.
[75] W. Gallagher, FTIR Analysis of Protein Structure, (1997) Accessed July 2018 http://www.chem.uwec.edu/Chem455_S05/Pages/Manuals/FTIR_of_proteins.pdf.
[76] M. Kumari, J.K. Maurya, M. Tasleem, P. Singh, R. Patel, Probing HSA-ionic liquid interactions by spectroscopic and molecular docking methods, J. Photochem. Photobiol. B 138 (2014) 27–35.
[77] C. Li, S. Kumar, C. Montigny, M. le Maire, A. Barth, Quality assessment of recombinant proteins by infrared spectroscopy. Characterisation of a protein aggregation related band of the Ca2+-ATPase, Analyst 139 (2014) 4231–4240.